

## Dominant Role of Subtropical Pacific Warming in Extreme Eastern Pacific Hurricane Seasons: 2015 and the Future

HIROYUKI MURAKAMI,<sup>a,b</sup> GABRIEL A. VECCHI,<sup>a,b</sup> THOMAS L. DELWORTH,<sup>a,b</sup>  
 ANDREW T. WITTENBERG,<sup>a</sup> SETH UNDERWOOD,<sup>c</sup> RICHARD GUDGEL,<sup>a</sup>  
 XIAOSONG YANG,<sup>d</sup> LIWEI JIA,<sup>a,b</sup> FANRONG ZENG,<sup>a</sup>  
 KAREN PAFFENDORF,<sup>a,b</sup> AND WEI ZHANG<sup>a,b</sup>

<sup>a</sup>NOAA/Geophysical Fluid Dynamics Laboratory, Princeton, New Jersey

<sup>b</sup>Atmospheric and Oceanic Sciences Program, Princeton University, Princeton, New Jersey

<sup>c</sup>Engility Corporation, Chantilly, Virginia

<sup>d</sup>University Corporation for Atmospheric Research, Boulder, Colorado

(Manuscript received 1 June 2016, in final form 8 September 2016)

### ABSTRACT

The 2015 hurricane season in the eastern and central Pacific Ocean (EPO and CPO), particularly around Hawaii, was extremely active, including a record number of tropical cyclones (TCs) and the first instance of three simultaneous category-4 hurricanes in the EPO and CPO. A strong El Niño developed during the 2015 boreal summer season and was attributed by some to be the cause of the extreme number of TCs. However, according to a suite of targeted high-resolution model experiments, the extreme 2015 EPO and CPO hurricane season was not primarily induced by the 2015 El Niño tropical Pacific warming, but by warming in the subtropical Pacific Ocean. This warming is not typical of El Niño, but rather of the Pacific meridional mode (PMM) superimposed on long-term anthropogenic warming. Although the likelihood of such an extreme year depends on the phase of natural variability, the coupled GCM projects an increase in the frequency of such extremely active TC years over the next few decades for EPO, CPO, and Hawaii as a result of enhanced subtropical Pacific warming from anthropogenic greenhouse gas forcing.

### 1. Introduction

The 2015 hurricane season in the eastern Pacific Ocean (EPO; Northern Hemisphere 180°–90°W, excluding the Atlantic Ocean) was extremely active. Twenty-seven tropical cyclones (TCs; maximum surface wind speed  $\geq 34$  kt; 1 kt  $\approx 0.51$  m s<sup>-1</sup>) were observed in the EPO in 2015 (Fig. 1a), the largest TC frequency since 1966 (Fig. 2a). The EPO can be divided into two subdomains: the eastern EPO (EEPO; Northern Hemisphere 140°–90°W) and the central

Pacific Ocean (CPO; Northern Hemisphere 180°–140°W).<sup>1</sup> Respectively, 18 and 9 TCs occurred in the EEPO and CPO in 2015 (Fig. 2b), which was the greatest TC frequency in the CPO since 1966 (the beginning of the satellite era, the point from which reliable TC frequency data in the eastern and central Pacific are available). This was the highest ratio of TCs in the CPO relative to the EEPO (50%; red line in Fig. 2b), even though the TC frequency in the EEPO was also high (although not a record). Moreover, four TCs approached the shores of Hawaii (defined by the red shading in Fig. 1) during the 2015 hurricane season (orange bar in Fig. 2c), which is the second largest number since 1966 (gray bars in Fig. 2c). This season followed the

Supplemental information related to this paper is available at the Journals Online website: <http://dx.doi.org/10.1175/JCLI-D-16-0424.s1>.

Corresponding author address: Hiroyuki Murakami, NOAA/Geophysical Fluid Dynamics Laboratory, 201 Forrestal Rd., Princeton, NJ 08540-6649.  
 E-mail: hir.murakami@gmail.com

<sup>1</sup>The National Hurricane Center and the Central Pacific Hurricane Center are in charge of monitoring and predicting TC activity in the EEPO and CPO, respectively, under the framework of the World Weather Watch (WWW) Programme of the World Meteorological Organization (WMO).

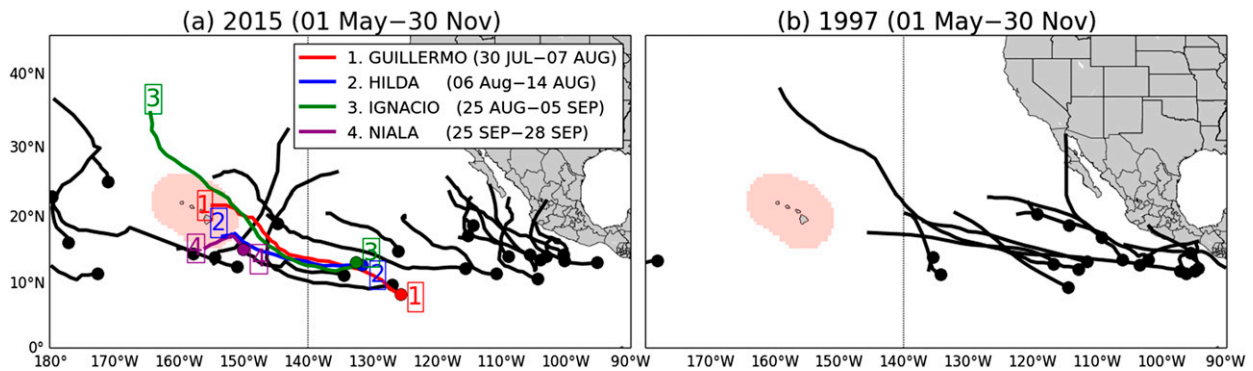


FIG. 1. TC tracks in (a) 2015 and (b) 1997. In (a), four TCs (red: Guillermo, blue: Hilda, green: Ignacio, and purple: Niala) approached the coastal region of Hawaii (red shading). Dots denote TC genesis locations.

active central Pacific TC season of 2014, in which three TCs also approached Hawaii (Murakami et al. 2015a)—the first observed instance in which three TCs approached the Hawaiian domain in two consecutive years.

Why was 2015 such an active in the EPO, CPO, and Hawaiian domain? Intrinsic ocean–atmosphere variability can result in strong variations in sea surface temperature (SST) and TC activity across the globe, including the EPO. In particular, a strong El Niño developed during the 2015 boreal summer season (see red box in Fig. 3a), and a number of scientific and media reports attributed the extreme TC number to the strong El Niño event (e.g., The Weather Channel 2015; Thompson 2015; Di Liberto 2015). Indeed, previous studies reported substantial effect of El Niño on TC activity in the EPO and CPO (e.g., Chu and Wang 1997; Collins and Roache 2011; Jin et al. 2014; Kim et al. 2014; Vecchi et al. 2014; Murakami et al. 2015a; Krishnamurthy et al. 2016). During the summer of a developing El Niño the mean location of TC genesis shifts to the west, and TCs tend to track farther westward in the EPO (Chu 2004), resulting in a tendency for increase TC density in the CPO (e.g., Kim et al. 2014; Vecchi et al. 2014)—although there are indications that the response of EPO TCs to El Niño exhibits nonlinearities (e.g., Krishnamurthy et al. 2016). Jin et al. (2014) reported an increase in intense TCs in the following summer of an El Niño peak. Chu and Wang (1997) reported that more TCs generate near Hawaii during El Niño developing years in the CPO. The correlation between TC frequency in the CPO and ENSO is 0.53 during 1966–97 (Chu and Clark 1999). However, little is known about the factors responsible for the interannual variation of TC frequency in the EEPO as well as in the EPO. Whitney and Hobgood (1997) reported that there is no relationship between El Niño–Southern Oscillation (ENSO) and TC frequency in the EPO. Chu (2004) reported that the average annual number of TCs in the EPO is 15.1 (15.0) during El Niño (La Niña) years,

indicating no difference between El Niño and La Niña years, based on the observed records from 1963 to 1993. Moreover, little is known about what controls extreme number of TC frequency in the EPO.

The Niño-3.4 SST anomaly (SSTA), a commonly used measure of the strength of El Niño, during May–November in 2015 was similar to that in 1997 (blue lines in Figs. 2a and 3b). However, TC frequencies in the EPO, CPO, and the Hawaiian domain were close to normal in 1997, while the 2015 EPO TC season was extremely active (Figs. 1b and 2). Why did more storms appear in 2015 than in 1997, despite similar central equatorial Pacific SSTA amplitude of the two El Niño events? In addition to El Niño, there are other modes of natural variability that may affect TC activity in the EPO and CPO. Murakami et al. (2015a) reported that the frequency of TCs approaching the Hawaiian domain has been found to be generally larger during the warm phases of ENSO (Chu and Wang 1997), Pacific decadal oscillation (PDO; Mantua et al. 1997; Wang et al. 2010; Lupo et al. 2008), interdecadal Pacific oscillation (IPO; Power et al. 1999; Folland et al. 2002; England et al. 2014), and the cold phase of the Atlantic multidecadal oscillation (AMO; Delworth and Mann 2000). Kucharski et al. (2011) documented that the tropical Atlantic warming during the late twentieth century might have led to a less Pacific warming through the Walker circulation. The reverse is true so that the cold phase of the AMO may lead more warming in the tropical EPO, which in turn leads to an active TC season in the basin. Indeed, above climate indices are all favorable for TC activity in the EPO in the 2015 summer season (colored lines in Fig. 2a; see the supplemental material for the definition of the climate indices). Therefore, based on historical relationships of climate indices to EPO TC activity alone, it is challenging to identify the cause of one active TC year.

In addition to the influence of internal variability on TC activity in the EPO and CPO, a number of previous

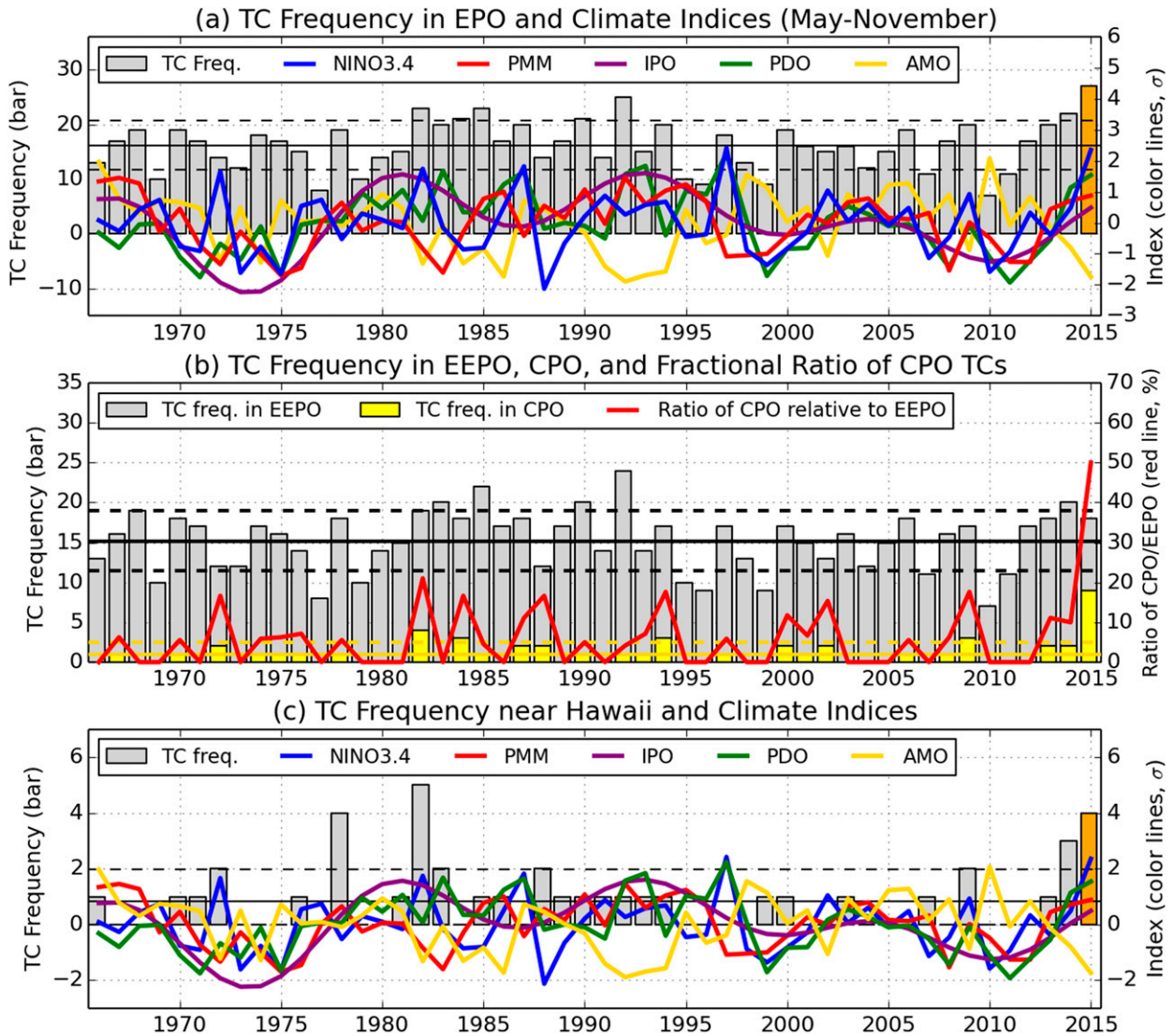


FIG. 2. (a) Yearly variability in the observed number of TCs in the EPO during the peak season of May–November, for the period 1966–2014 (gray bars) and 2015 (orange bar). Colored lines denote climate indices, in units of standard deviation, for ENSO (Niño-3.4, blue), PMM (red), IPO (purple), PDO (green), and AMO (yellow). For details on the climate indices and methods used to detect them (see the supplemental material). (b) Yearly variability in the number of TCs in the EEPO (gray bars) and CPO (yellow bars), including the fractional ratio of TC frequency in the CPO relative to EEPO (red line). (c) As in (a), but for frequency of storms approaching the coastal regions of Hawaii. Dashed lines indicate  $\pm 1\sigma$  for TC frequency, and the solid black line indicates mean value for TC frequency.

studies reported projected increase in TC frequency in the CPO due to greenhouse gas–induced global warming (Li et al. 2010; Murakami et al. 2013; Knutson et al. 2015). The projected increase is principally associated with a northwestward shift of EPO TC tracks in the southeast of the Hawaiian Islands, where climate models robustly predict greater warming than the rest of the tropics (Vecchi and Soden 2007; Murakami et al. 2013). Murakami et al. (2015a) investigated the influence of anthropogenic forcing and natural variability on the abnormal TC frequency near Hawaii in 2014, using a suite of climate simulations.

Murakami et al. (2015a) conclude that the extremely active 2014 Hawaiian hurricane season was made substantially more likely by anthropogenic forcing, but that natural variability (El Niño in particular) was also involved. In the present study, we build on methodology of Murakami et al. (2015a) to explore the factors responsible for the extremely active TC season for the EPO, CPO, and Hawaii in 2015. First we analyze observations and model simulations in order to understand effect of tropical ( $10^{\circ}\text{S}$ – $10^{\circ}\text{N}$ ,  $170^{\circ}$ – $80^{\circ}\text{W}$ ) and subtropical ( $10^{\circ}$ – $35^{\circ}\text{N}$ ,  $150^{\circ}$ – $100^{\circ}\text{W}$ ) SST anomalies on TC frequency in the EPO.

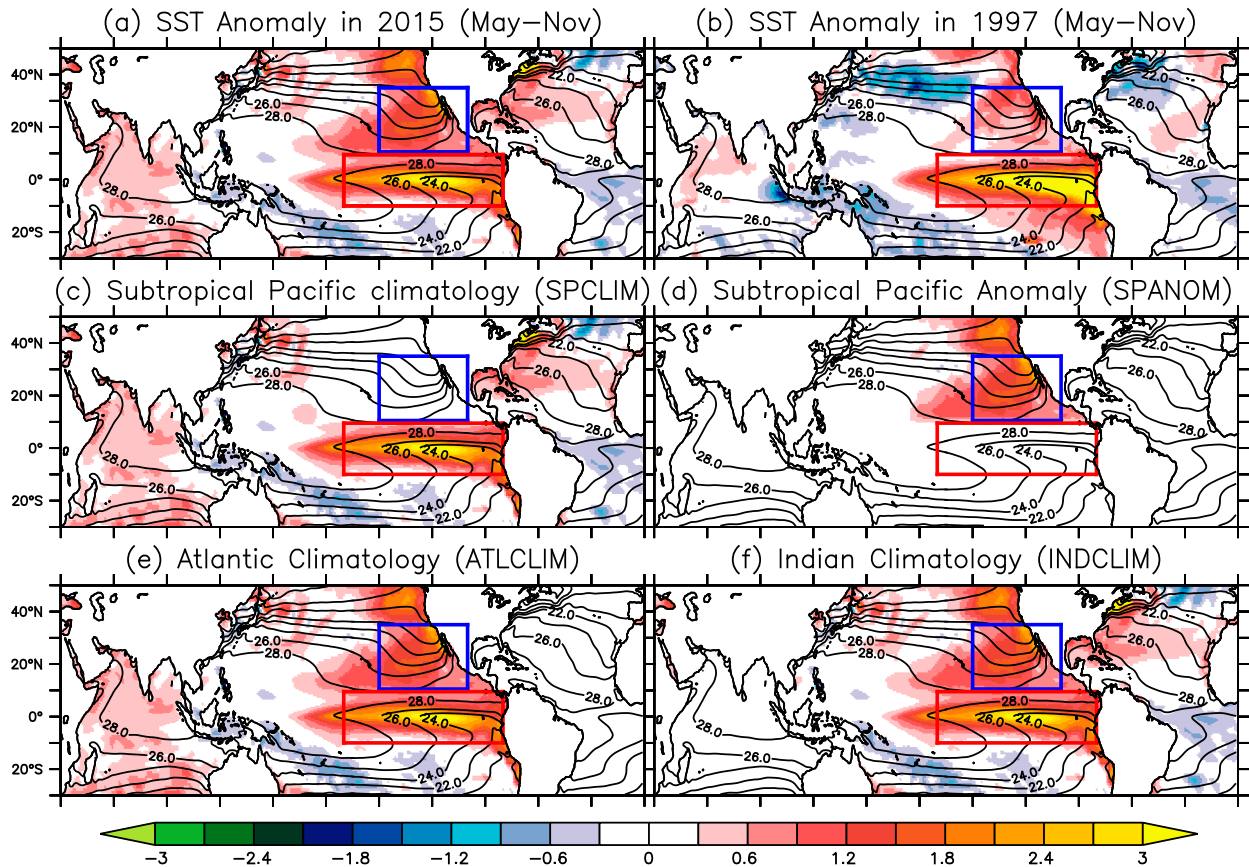


FIG. 3. Observed SSTA (shading; K) in (a) 2015 and (b) 1997 during May–November relative to the 1980–2015 mean (contours; °C). Also shown is idealized SSTA prescribed for the sensitivity experiments: (c) SPCLIM, observed 2015 SSTA except climatological mean SST in the subtropical central Pacific; (d) SPANOM, observed 2015 SSTA except climatological mean SST globally outside of the subtropical central Pacific; (e) ATLCLIM, observed 2015 SSTA except climatological mean SST in the Atlantic Ocean; and (f) INDCLIM, observed 2015 SSTA except climatological mean SST in the Indian Ocean. The blue (red) rectangle denotes the subtropical (tropical) region defined in this study.

Also, we investigate possible future changes in the probability of occurrence of extremely active TC year such as 2015 using a suite of climate simulations.

The remainder of this paper is organized as follows. Section 2 describes the models and data used in this study. Section 3a analyzes observations. Section 3b focuses on a possible cause of the extremely active 2015 TC year using idealized experiments under the framework of seasonal forecast. Sections 3c and 3d investigate possible impact of anthropogenic warming and natural variability on frequency of occurrence for extremely active TC year. Finally, section 4 provides conclusions and a discussion of the results.

## 2. Methods

### a. Observational datasets

We first analyze observed TC frequency along with observed large-scale parameters in the EPO (see section 3a).

The observed TC best-track data were obtained from the National Hurricane Center's best track database (HURDAT2; Landsea and Franklin 2013) as archived in the International Best Track Archive for Climate Stewardship (IBTrACS; Knapp et al. 2010) for the period 1966–2014. The data before 1966 are less reliable because satellite observations were not sufficiently available for compiling TC data (Frank 1987). For the 2015 TC data, the Unisys Corporation website (Unisys 2016) is used in this study. We also used the Met Office Hadley Centre Sea Ice and SST product (HadISST1.1; Rayner et al. 2003) as observed SST for the period 1966–2015. For the precipitation data, Climate Prediction Center (CPC) Merged Analysis of Precipitation (CMAP; Xie and Arkin 1997) was used for the period 1979–2015. For the atmospheric data, the Japanese 55-year Reanalysis (JRA-55; Kobayashi et al. 2015) for the period 1966–2015 was used. For the subsurface ocean temperature data, we used the GFDL ensemble coupled data assimilation (ECDA; Zhang and Rosati 2010; Chang et al. 2013) for the period 1966–2015.

To elucidate the potential influence of natural variability on the frequency of TCs in the EPO, we use above observations for computing indices of ENSO, the PDO (Mantua et al. 1997), the IPO (Power et al. 1999; Folland et al. 2002; England et al. 2014), the Pacific meridional mode (PMM; Chiang and Vimont 2004), and the AMO (Delworth and Mann 2000). The detailed calculation for the climate indices and spatial patterns are described in the supplementary information.

### b. Models and TC detection method

We used the Geophysical Fluid Dynamics Laboratory (GFDL) Forecast-Oriented Low Ocean Resolution Model (FLOR; Vecchi et al. 2014). FLOR comprises approximately 50-km mesh atmosphere and land components, and approximately 100-km mesh sea ice and ocean components. Any simulations or forecasts by FLOR were conducted using “flux adjustment,” which adjusts the model’s air–sea fluxes of momentum, enthalpy, and freshwater to bring the long-term climatology of SST and surface wind stress closer to the observations (Vecchi et al. 2014). Simulation characteristics, global climate sensitivity, and forecast performance of FLOR are documented in a series of manuscripts (e.g., Vecchi et al. 2014; Winton et al. 2014; Msadek et al. 2014; Jia et al. 2015; Yang et al. 2015a; Delworth et al. 2015; Zhang and Delworth 2015; Krishnamurthy et al. 2015, 2016; Murakami et al. 2015b, 2016a,b; Zhang et al. 2016a,b). We also conducted idealized seasonal predictions using the atmospheric component of FLOR [i.e., Atmosphere Model, version 2.5 (AM2.5)] by prescribing different SSTA spatial patterns in order to address relative importance of regional SSTA on the active 2015 TC season.

Model-generated TCs were detected directly from 6-hourly output, using the following tracking scheme developed in Harris et al. (2016), as implemented in Murakami et al. (2015b). In the detection scheme, the flood fill algorithm is applied to find closed contours of a specified negative sea level pressure (SLP) anomaly with a warm core. The TC detection must maintain warm core and wind criteria of  $15.75 \text{ m s}^{-1}$  for at least 36 consecutive hours. Because FLOR and AM2.5 have systematic model biases in basinwide TC frequency, the simulated TC counts are calibrated using observed data: simulated TC counts are scaled by the ratio of the observed and predicted mean values for the period 1980–2015.

Throughout this study, we evaluate TC frequency and large-scale parameters during May–November because the official hurricane season defined by the

U.S. National Weather Service extends from May to November (Chu 2004).

### c. Retrospective seasonal forecasts

We first evaluate retrospective/real-time seasonal forecasts in order to evaluate if FLOR has skill in predicting an active TC season in 2015 during the peak TC season (May–November) as well as interannual variation of TC frequency. We conducted 12-member ensemble forecasts initialized on 1 May for each year in the period 1980–2015. The seasonal predictions were performed for a 12-month duration for each ensemble member. The initial conditions for ocean and sea ice were derived from the coupled ensemble Kalman filter (EnKF; Zhang and Rosati 2010) data assimilation system developed for the GFDL Climate Model, version 2.1 (CM2.1; Delworth et al. 2006; Gnanadesikan et al. 2006; Wittenberg et al. 2006). However, the initial conditions for atmosphere and land components were not available because we do not have an assimilation system for them so far. Therefore, they were built through SST-forced atmosphere–land-only simulations using the atmospheric components of FLOR.

Figure 4 shows prediction skill for TC frequency for each ocean basins along with landfall frequency over the Hawaiian domain. FLOR could predict an active TC season in 2015 in addition to the reasonable interannual variation of TC frequency. The correlation between predicted and observed TC frequency is significant for the EPO ( $r = 0.63$ ), EEPO ( $r = 0.56$ ), CPO ( $r = 0.54$ ), and the Hawaiian domain ( $r = 0.53$ ). Moreover, FLOR could predict extreme TC frequency in 2015 for all of the ocean basins. The reasonable forecast skill for other ocean basins (e.g., North Atlantic and western North Pacific) is also documented in Vecchi et al. (2014), Murakami et al. (2016a,b), and Zhang et al. (2016b). The high skill instills greater confidence for the use of the model to address the factors responsible for the active TC year of 2015. Meanwhile the observed TC count in 2015 for the CPO was out of range of the ensemble spread (Fig. 4c). It is not clear so far if the model deficiency is due to unpredictable stochastic processes in nature, or just because the model misses some processes related to the extreme TC frequency.

### d. The 1860- and 1990-control and multidecadal simulations

To isolate effect of natural variability and anthropogenic forcing, we conducted control simulations and two types of 35-member ensemble multidecadal simulations using FLOR. We first generated 3500-yr control climate simulations (Murakami et al. 2015a; Yang et al. 2015b; Jia et al. 2016) using FLOR by prescribing radiative forcing and

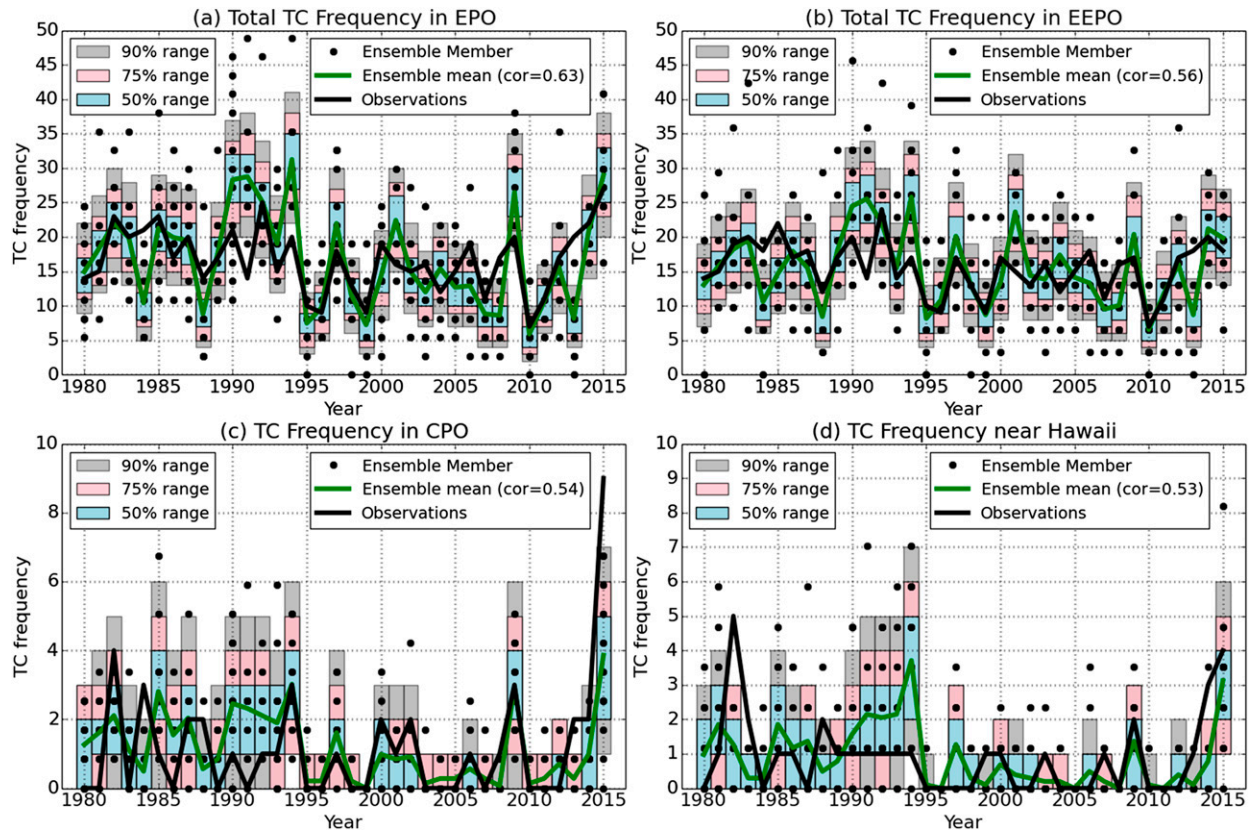


FIG. 4. Retrospective forecasts of basinwide TC frequency in the (a) EPO, (b) EEPO, and (c) CPO, and (d) near Hawaii, during the peak season of May–November initialized from May, for the period 1980–2015 using FLOR. The black line indicates observed TC frequency, green line indicates the mean forecast value, and shading indicates the confidence intervals computed by convolving interensemble spread based on the Poisson distribution. The dots indicate prediction value for each ensemble member. The number in parentheses in the top-right legend for each panel indicates the rank correlation coefficient between the observed and mean values.

land-use conditions representative of the year 1860 (1860-control). In addition, we generated 500-yr control climate simulations by prescribing conditions representative of the year 1990 (1990-control; Vecchi et al. 2014). These control experiments are free run in which reasonable internal variability of PDO (Zhang and Delworth 2015), ENSO (Vecchi et al. 2014; Krishnamurthy et al. 2016; Zhang et al. 2016a), and other internal variability of IPO and AMO are simulated given an arbitrary initial condition. The mean difference between the two control experiments is thought to be due to effect of anthropogenic forcing.

Two types of multidecadal simulations were conducted for the period 1941–2040 (Fig. 5; Jia et al. 2016; Murakami et al. 2015a; Yang et al. 2015b). One of them is the all forcing experiment (AllForc), which uses prescribed phase 5 of the Coupled Model Intercomparison Project (CMIP5) historical natural and anthropogenic forcing and aerosols up to 2005, and future projected levels based on the CMIP5 representative concentration pathway 4.5 (RCP4.5) scenario from 2006 to 2040. In the AllForc experiment, historical volcanic radiative forcing was also

prescribed up to 2005; however, no volcanic forcing was prescribed after 2006. In an event of volcanic forcing, global mean surface temperature decreases (Fig. 5). Another simulation is the 1941 forcing experiment (1941Forc), which uses anthropogenic forcing (e.g., greenhouse gases, ozone, and sulfate) fixed at the CMIP5 historical scenario 1941 level but time-varying CMIP5 natural forcings (e.g., solar forcing) from 1941 to 2040. Except for the differences in anthropogenic forcings, the 1941Forc and AllForc experiments use the same experimental settings (initial conditions, model settings, etc.). These multidecadal simulations were not initialized to observed estimates of the climate state, but are initialized from a set of experiments that begin in 1861; that is, simulated internal variability generally was out of phase among the various ensemble members and observations (Murakami et al. 2015a; Yang et al. 2015b; Jia et al. 2016).

#### e. Empirical probability of exceedance

To estimate the potential probability of occurrence for the extreme TC-incidence years such as 2015, we

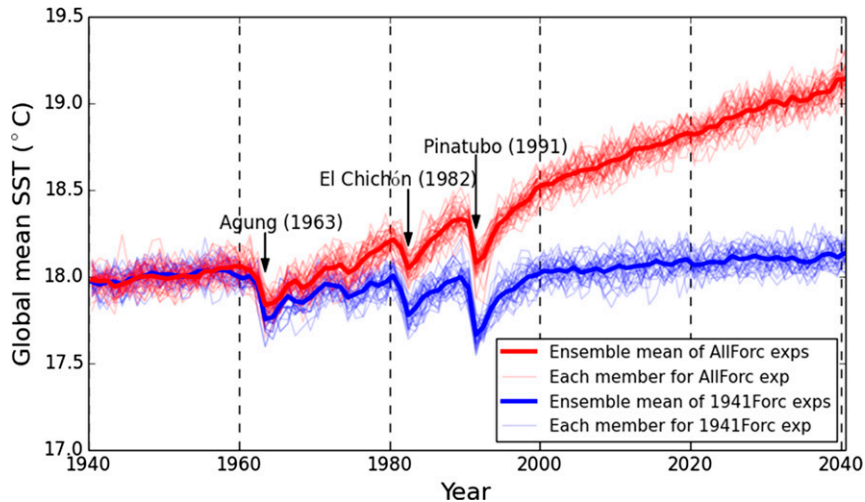


FIG. 5. Interannual variation of global mean SST simulated by AllForc multidecadal experiment for the period 1941–2040. The thin red lines show simulated global mean SST for each ensemble member. The thick red line shows the ensemble mean value. Blue lines are the same as the red lines, but for the experiment with the constant forcing representative of 1941Forc experiment. Black arrows denote the major historical volcanic events. The simulated internal variability is out of phase among the ensemble members, whereas the ensemble mean shows a significant positive trend due to the response of anthropogenic forcing along with a few abrupt decreases due to volcanic forcing. For each 20-yr period, 700 ( $20 \text{ yr} \times 35 \text{ ensemble members}$ ) samples are obtained to compute  $P(x)$ . Reprinted from Murakami et al. (2015a) with modifications.

examine the empirical probability of exceedance for the frequency (Murakami et al. 2015a):

$$P(x) = \frac{\text{No. of years with TCs} \geq x}{\text{Total No. of years}}, \quad (1)$$

where  $x$  is the annual number of TCs. For example,  $P(27)$  represents the probability of occurrence of a year with 27 or more TCs. For the 1860- (1990-) control experiments, we compute  $P(x)$  using all 3500 (500) simulated years. To elucidate intercentennial variability, we compute  $P(x)$  for each 100-yr period.

For the multidecadal experiments,  $P(x)$  was computed for each 20-yr period from 1941 onward, yielding 700 ( $=20 \times 35$ ) samples from which to calculate  $P(x)$  (Fig. 5). Because the simulated internal variability is out of phase among the ensemble members, we can estimate for each 20-yr period the conditional probability  $P(x | Y_{\pm})$  under any phase of a natural mode of variability (i.e.,  $Y_+$  or  $Y_-$ ). We define a positive (or negative) phase of ENSO, PDO, IPO, PMM, and AMO when the May–November index amplitude exceeds one standard deviation (or falls below minus one standard deviation) and estimate the range of  $P(x)$  between the two phases.

#### f. Statistical significance test

To assess statistical significance for the simulated mean difference between 1860- and 1990-control experiments in

terms of simulated TC frequency as well as TC density and large-scale parameters for each grid box, the bootstrap method proposed by Murakami et al. (2013) is applied. We avoid using the Student's  $t$  test to address statistical significance because TC frequency and TC density are not necessarily subject to a Gaussian distribution, but rather to a Poisson distribution. Therefore, a nonparametric method is preferable in these cases. First, the two datasets of 1860-control (3500 yr) and 1990-control (500 yr) experiments are combined (4000 yr). Second, we perform 1000 resamplings of data, in which data were randomly picked from the combined data with replacement. The sampled data are assigned arbitrarily to the 1860-control or 1990-control group with the same sample size as the original data (i.e., 3500 and 500 yr, respectively); thereby, the sampling distribution is computed based on the difference between the resampled 1860-control and 1990-control groups. Finally, the  $P$  value can be computed from the difference of the original data relative to the sampling distribution.

### 3. Results

#### a. Observed analysis for the extremely active 2015 TC year

As briefly mentioned in introduction, historical record of 27 (9) TCs are observed in the EPO (CPO) during

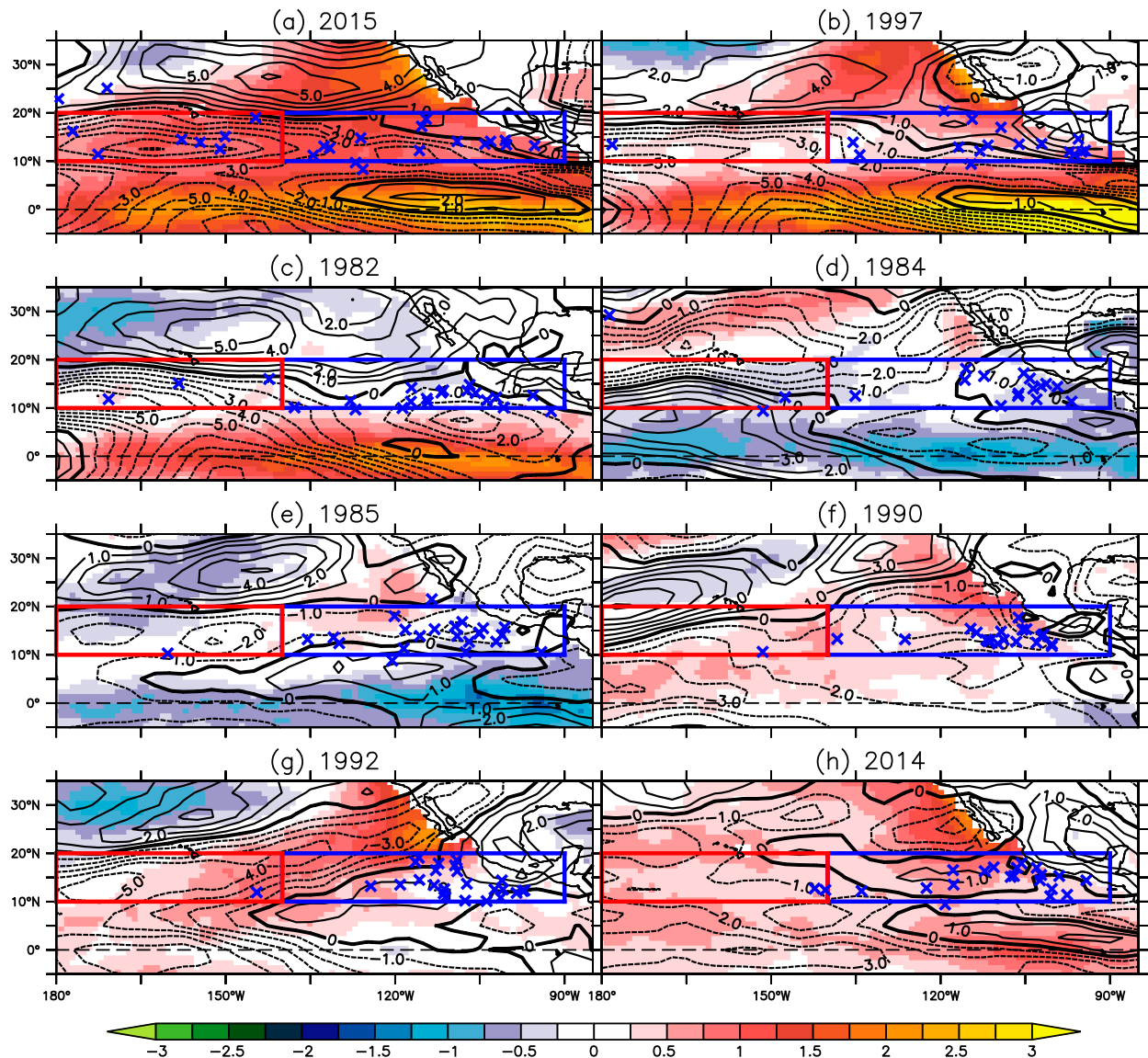


FIG. 6. Observed anomaly of magnitude of vertical wind shear (contours;  $\text{m s}^{-1}$ ) superimposed on the observed SSTa (shadings; K) and observed locations of TC genesis (blue crosses) during May–November. Shown are for the seven extremely active TC years of (a) 2015, (c) 1982, (d) 1984, (e) 1985, (f) 1990, (g) 1992, and (h) 2014 in addition to the moderately above normal TC year of (b) 1997 for comparison. The blue and red rectangle domains are defined as the MDRs for TC genesis for the EEPO and CPO, respectively.

2015 summer season (Figs. 1 and 2). The mean TC frequency and one standard deviation  $\sigma$  are, respectively, 16.2 and 4.5 for the EPO, whereas those are 1.5 and 1.0 for the CPO. Therefore, anomaly of TC frequency in 2015 is  $+2.4\sigma$  for the EPO (and  $+7.5\sigma$  for the CPO), indicating extreme number of TC frequency in 2015. The Niño-3.4 index was also high ( $+2.36\sigma$ ) in the 2015 summer season (Fig. 2a), resulting from extremely warm subsurface ocean conditions in the equatorial EPO in the 2015 summer season. This index was the second highest since 1966, trailing slightly that of 1997 ( $2.42\sigma$ ). This observed co-occurrence might suggest that the odds

of an extremely active 2015 TC season in the EPO and CPO were substantially enhanced by the development of this substantial El Niño event.

However, when we focus on the historical record of extremely active TC years in the EPO, they do not always emerge during an El Niño year (Figs. 2a and 6). We define extremely active TC years as those when the anomaly of TC frequency exceeds  $+1.0\sigma$  (which leads to the selection of 1982, 1984, 1985, 1990, 1992, 2014, and 2015). Among the seven extreme years, only two years (1982 and 2015; 29%) were during El Niño event (El Niño event is defined when the Niño-3.4 index exceeds  $+1.0\sigma$ ;

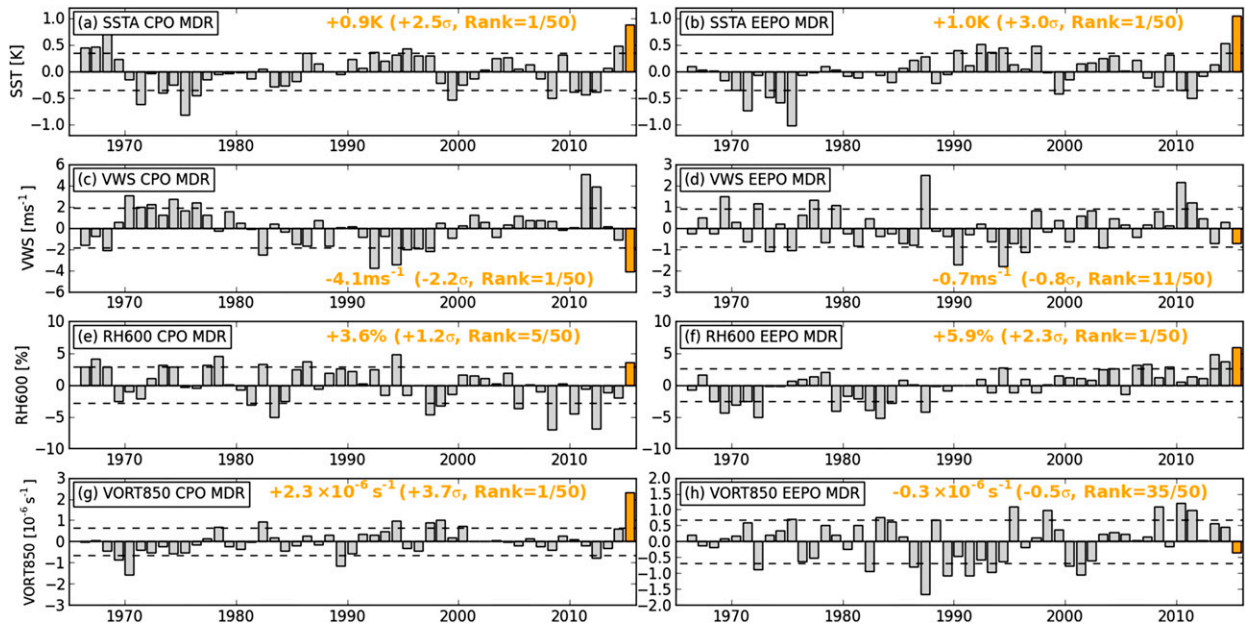


FIG. 7. Yearly variability in the observed area mean of large-scale parameters over the (left) CPO and (right) EEPO MDRs. Plotted are (a),(b) SSTA (K), (c),(d) vertical wind shear (VWS;  $\text{m s}^{-1}$ ), (e),(f) relative humidity at 600 hPa (RH600; %), and (g),(h) relative vorticity at 850 hPa (VORT850;  $10^{-6} \text{ s}^{-1}$ ). Orange bars highlight the area mean values for 2015. Percent values in orange specifies the mean value for the 2015 summer season. The information in parentheses denotes the anomaly for 2015 in standard deviation and the rank based on the 1966–2015 values.

blue line in Fig. 2a). Meanwhile, there were two La Niña years (1984 and 1985) in the extreme TC years. Therefore, a full exploration of the historical record suggests a much more complex relationship between El Niño and extremely active TC years in the EPO, and it is likely that a strong El Niño, like 2015, is not the only factor responsible for the emergence of extremely active TC years—even though some intense El Niño years are associated with extremely active EPO TC seasons (e.g., 1982 and 2015).

Generally, TC genesis in the EPO is most common in the latitudinal belt between  $10^{\circ}$  and  $20^{\circ}\text{N}$  (Fig. 6) whereas the intertropical convective zone (ITCZ) is located to the south of this latitudinal belt. We define the domain of most frequent TC genesis as the main development region (MDR). In the EEPO, MDR is defined as the blue box as shown in Fig. 6. This MDR was also defined in the previous study (Wu and Chu 2007). Although TC genesis is rare in the CPO, most of the TC genesis occurred in the red box in Fig. 6, and it is defined as the MDR for the CPO in this study. The 2015 summer season was characterized as weaker vertical wind shear in the both MDRs along with warmer central Pacific (Fig. 6a). Specifically, vertical wind shear was historically low in the CPO MDR (Fig. 7c), and SSTA was historically high in both the EEPO and CPO MDRs (Figs. 7a,b). Moreover, mean midlevel relative humidity

was historically high in the EEPO MDR (Fig. 7f), and mean low-level vorticity was also the highest over the CPO MDR (Fig. 7g). These results highlight that large-scale environment was extremely favorable for TC genesis during the 2015 summer seasons for both the EEPO and CPO MDRs.

In addition to the near-equatorial SSTA (e.g., Niño-3.4), subtropical SSTA ( $10^{\circ}$ – $35^{\circ}\text{N}$ ,  $150^{\circ}$ – $100^{\circ}\text{W}$ ) was also extremely high during the 2015 summer season (blue domain in Fig. 3a). To clarify the relative importance of the subtropical Pacific SSTA versus tropical Pacific SSTA, we can compare the TC activity of each season to the amplitude of tropical ( $10^{\circ}\text{S}$ – $10^{\circ}\text{N}$ ,  $170^{\circ}$ – $80^{\circ}\text{W}$ ) and subtropical ( $10^{\circ}$ – $35^{\circ}\text{N}$ ,  $150^{\circ}$ – $100^{\circ}\text{W}$ ) SSTAs (Figs. 8a–c). The radius of a circle is proportional to TC frequency, and red color highlights an extreme TC year defined as when the anomaly of TC frequency exceeds one standard deviation. For the EPO and EEPO (Figs. 8a,b), higher subtropical SSTA tends to show more frequent extreme TC years than the higher tropical SSTA does. Among the seven extreme TC years, four years show subtropical warming for the EPO (57%; Fig. 8a)—a higher fraction than those co-occurring with tropical warming associated with El Niño (i.e., two out of seven extreme years; 29%). However, there are exceptions, like 1984 and 1985, when both tropical and subtropical SSTAs were not large, indicating that SSTA is not only

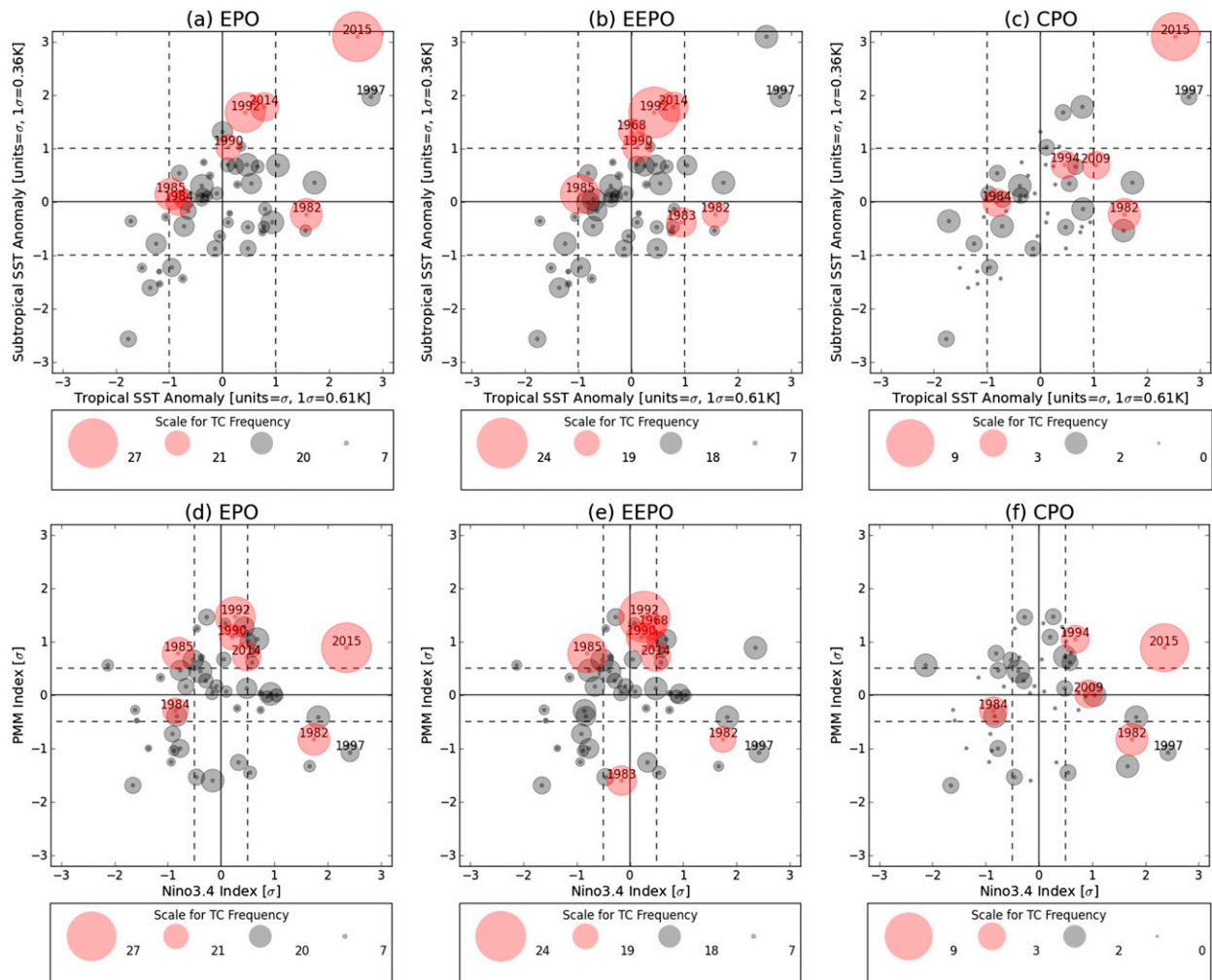


FIG. 8. Scatterplots for the observed tropical SSTA ( $10^{\circ}\text{S}$ – $10^{\circ}\text{N}$ ,  $170^{\circ}$ – $80^{\circ}\text{W}$ ) vs the subtropical SSTA ( $10^{\circ}$ – $35^{\circ}\text{N}$ ,  $150^{\circ}$ – $100^{\circ}\text{W}$ ) during May–November for each year of 1966–2015, for (a) EPO, (b) EEPO, and (c) CPO. The size of circle is proportional to the observed TC genesis frequency for the plotted year. Red circles highlight the years with TC frequency more than one standard deviation. (d)–(f) As in (a)–(c), but for scatterplots for the observed Niño-3.4 index vs PMM index.

the factor for the emergence of extreme TC years (or perhaps indicating the role of stochastic processes in seasonal TC activity). On the other hand, extreme years of the CPO TCs show a closer relationship with tropical SSTA in the observations than with subtropical SSTA (Fig. 8c), which is consistent with a previous study (Chu and Clark 1999). Three out of seven extreme years (43%) show extreme TC years in CPO during tropical warming years, whereas one out of seven extreme years (14%) shows extreme TC years in CPO during subtropical warming years.

The positive SSTA over the subtropical EPO in 2015 is related to the positive phase of the PMM. The PMM is the internal coupled mode of ocean–atmosphere variability, involving coupling between winds, evaporation, and ocean temperatures in the tropical and subtropical

EPO (Chiang and Vimont 2004; see Fig. S4 in the supplemental material). The positive PMM phase is characterized by a marked warming over the subtropical EPO and a cooling over the tropical EPO (Fig. S4b). The subtropical SSTA related to the positive PMM generally peaks in the boreal spring (e.g., April–May), and it generally fades out during the boreal summer (e.g., July–September) in the EPO (Chiang and Vimont 2004). The PMM mode is also similar to the North Pacific mode (NPM; Deser and Blackmon 1995), which refers to the second mode of SST structures over the Pacific domain  $20^{\circ}\text{S}$ – $60^{\circ}\text{N}$ . Hartmann (2015) reported that positive NPM is characterized by a maximum positive SST anomaly centered round  $45^{\circ}\text{N}$  in the North Pacific along with the subtropical Pacific warming that is similar to the positive PMM pattern. Hartmann (2015)

reported that the recent large positive NPM phase might have caused the severe winter in North America in 2013/14. The positive PMM is also thought to trigger some El Niño developing events (Chang et al. 2007; Zhang et al. 2009).

When we redraw Figs. 8a–c for the relationship between the Niño-3.4 and PMM indices (Figs. 8d–f), we obtain almost the same relationships as when the tropical and subtropical SSTs are used (Figs. 8a–c): Higher PMM index tends to show more extreme TC years in the EPO and EEPO than the Niño-3.4 index does. However, the large difference is apparent for 1997. Although the PMM index was positive during the 1997 boreal spring, it turned negative ( $-1.1\sigma$ ) during the 1997 boreal summer, in spite of the slightly positive SSTA in the subtropics. On the other hand, the subtropical Pacific warming related to the positive PMM in 2015 remained throughout the summertime. We speculate that the difference in the subtropical warming may be one of the critical factors separating the active TC season in 2015 and normal TC season in 1997. To assess this hypothesis, we perform a series of idealized simulations in the next section.

Before moving to the model simulations, it is worthwhile comparing the impact of tropical SST warming and subtropical SST warming on the large-scale parameters in observations. For this purpose, we make two composites using observations. One of them is the composite of the large-scale parameters using the years with the subtropical SSTA more than  $+0.5\sigma$  but with the tropical SSTA less than  $+0.5\sigma$  (SUB; 1969, 1972, 1982, 1983, 1987, 1991, 2002, and 2006). Another are composites for those years with the tropical SSTA more than  $+0.5\sigma$  but with the subtropical SSTA less than  $+0.5\sigma$  (TRP; 1967, 1968, 1986, 1990, 1992, 1994, 1996, 2003, and 2004). Figure 9 shows composite of anomalies for SST, precipitation, ocean thermal energy potential (OTEP; Gray 1975), midlevel relative humidity, vertical wind shear, and low-level relative vorticity for the SUB (Fig. 9, left) and TRP (Fig. 9, right). Note that the composites for precipitation were made from 1979 because the CMAP data are available from 1979. OTEP ( $\text{cal cm}^{-2}$ ;  $1 \text{ cal} = 4.184 \text{ J}$ ) is a measure of warmth of subsurface ocean defined as follows:

$$\text{OTEP} = \int_{\text{surface}}^{60\text{m, or where } T=26^\circ\text{C}} \rho_w c_w (T - 26) dz, \quad (2)$$

where  $T$  is ocean temperature ( $^\circ\text{C}$ ),  $\rho_w$  is ocean density ( $1 \text{ gm cm}^{-3}$ ), and  $c_w$  is the specific heat of water ( $1 \text{ cal g}^{-1} \text{ }^\circ\text{C}$ ). A large OTEP value is favorable for TC development through abundant thermal energy without losing energy by the storm-induced cold wake (Gray 1975).

Overall, all of the variables show more favorable conditions for TC genesis in the SUB composites relative to

the TRP composites over the MDRs: larger precipitation (Figs. 9c,d), higher OTEP (Figs. 9e,f), higher relative humidity (Figs. 9g,h), weaker vertical wind shear (Figs. 9i,j), and larger positive vorticity (Figs. 9k,l). The composite results for the vertical wind shear are consistent with the previous study of Larson et al. (2012). Therefore, the subtropical warming brings more favorable large-scale conditions for TC genesis than the tropical Pacific warming does. Specifically, the composite for precipitation (Figs. 9c,d) suggests that the ITCZ shifts poleward during the subtropical warming years relative to the climatological mean, whereas the ITCZ slightly shifts equatorward during the tropical warming years. Although it is in the model world, Merlis et al. (2013) reported that the simulated location of the ITCZ is critical for simulated TC frequency, with an increase in TC frequency as the ITCZ shifts poleward. Although sample size is limited for observations, the 500-yr 1990-control simulation with more samples shows consistent results (figure not shown).

In the next section, we further investigate relative importance of the subtropical Pacific and tropical SSAs, in addition to the SSTAs in other ocean basins, to the extreme TC year of 2015 under the framework of seasonal forecast.

### b. Idealized retrospective seasonal forecast

As mentioned in the previous section, the spatial pattern and magnitudes of SSTAs in the 2015 summer season resembles those observed in 1997 (Figs. 3a,b): marked warming in the tropical and subtropical EPO and Indian Ocean and slight cooling in the tropical North Atlantic. To assess the relative importance of the above regional SSTAs to the active TC season in 2015, we conduct idealized 12-member ensemble predictions using the atmosphere component of FLOR (i.e., AM2.5) initialized on 1 May 2015, and driven by various prescribed SSTA patterns. The three control experiments are named CLIMSST, ANOM1997, and ANOM2015, in which SSTAs are set to zero, 1997 observed values (shading in Fig. 3b), and 2015 FLOR predicted values (shading in Fig. 3a), respectively. Figure 10 shows the predicted TC frequency in the EPO, EEPO, CPO, and near Hawaii. The ANOM2015 shows markedly more TCs than the CLIMSST and ANOM1997 experiments, consistent with the observations and FLOR predictions (Figs. 1, 2, and 4). The experiments ATLCLIM and INDCLIM resemble the ANOM2015, except that SSTAs are set to zero over the Atlantic Ocean and Indian Ocean, respectively (Figs. 3e,f). These experiments show only small differences from ANOM2015 in terms of simulated TC frequency, indicating that the SSTAs in these basins do not strongly influence the 2015 TC activity in the model predictions. The ATLCLIM experiment

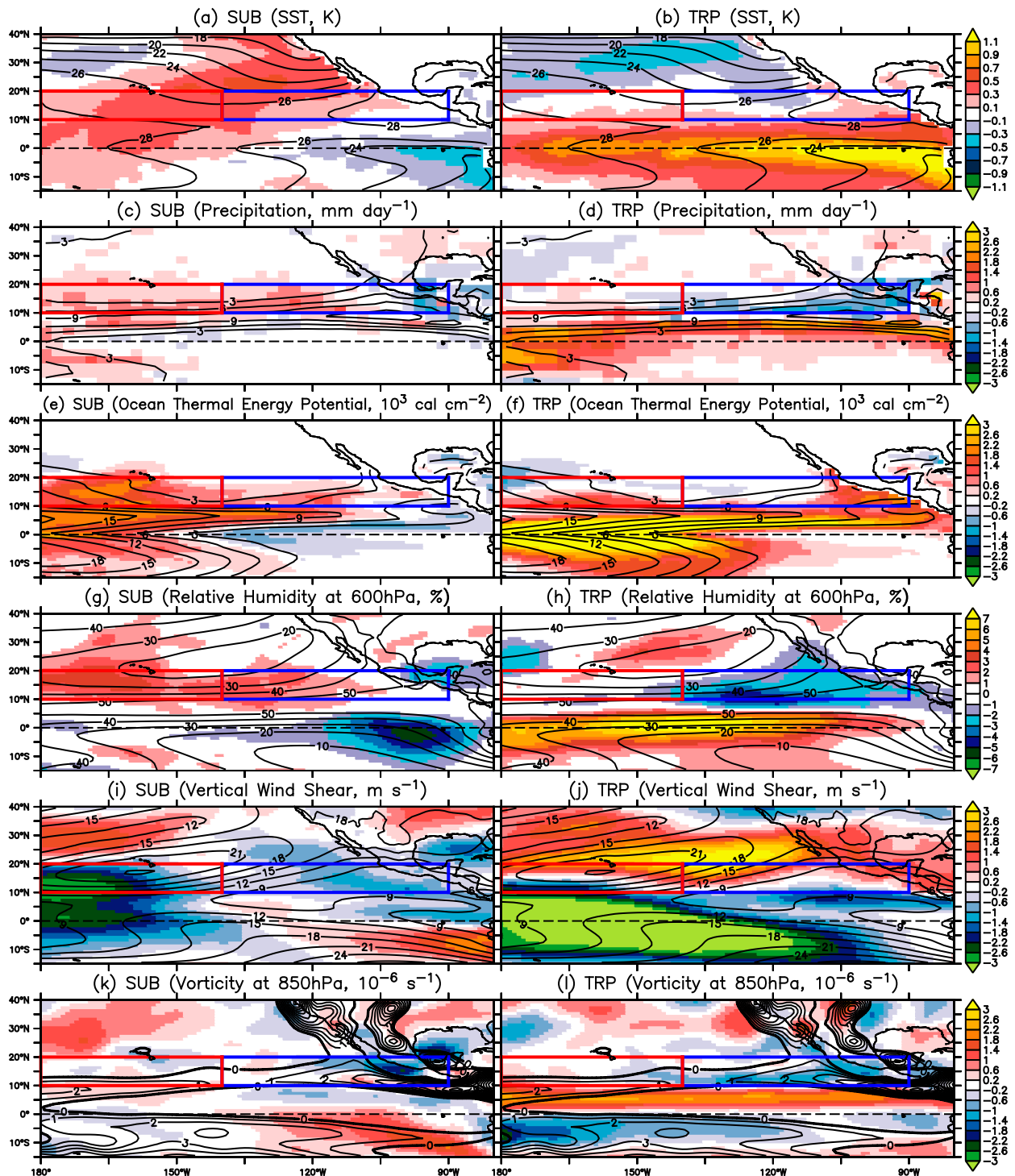


FIG. 9. Composite of anomaly (shading) of the large-scale parameters during (left) the year with the subtropical Pacific warming (SUB) and (right) the years with the tropical Pacific warming (TRP). Contours denote climatological mean value for 1966–2015. Shown are (a), (b) SST (K), (c), (d) precipitation (only for 1979–2015;  $\text{mm day}^{-1}$ ), (e), (f) ocean thermal energy potential ( $10^3 \text{ cal cm}^{-2}$ ), (g), (h) relative humidity at 600 hPa (%), (i), (j) vertical wind shear ( $\text{m s}^{-1}$ ), and (k), (l) relative vorticity at 850 hPa ( $10^{-6} \text{ s}^{-1}$ ). The blue and red rectangle domains are defined as the MDRs for TC genesis for the EEPO and CPO, respectively.

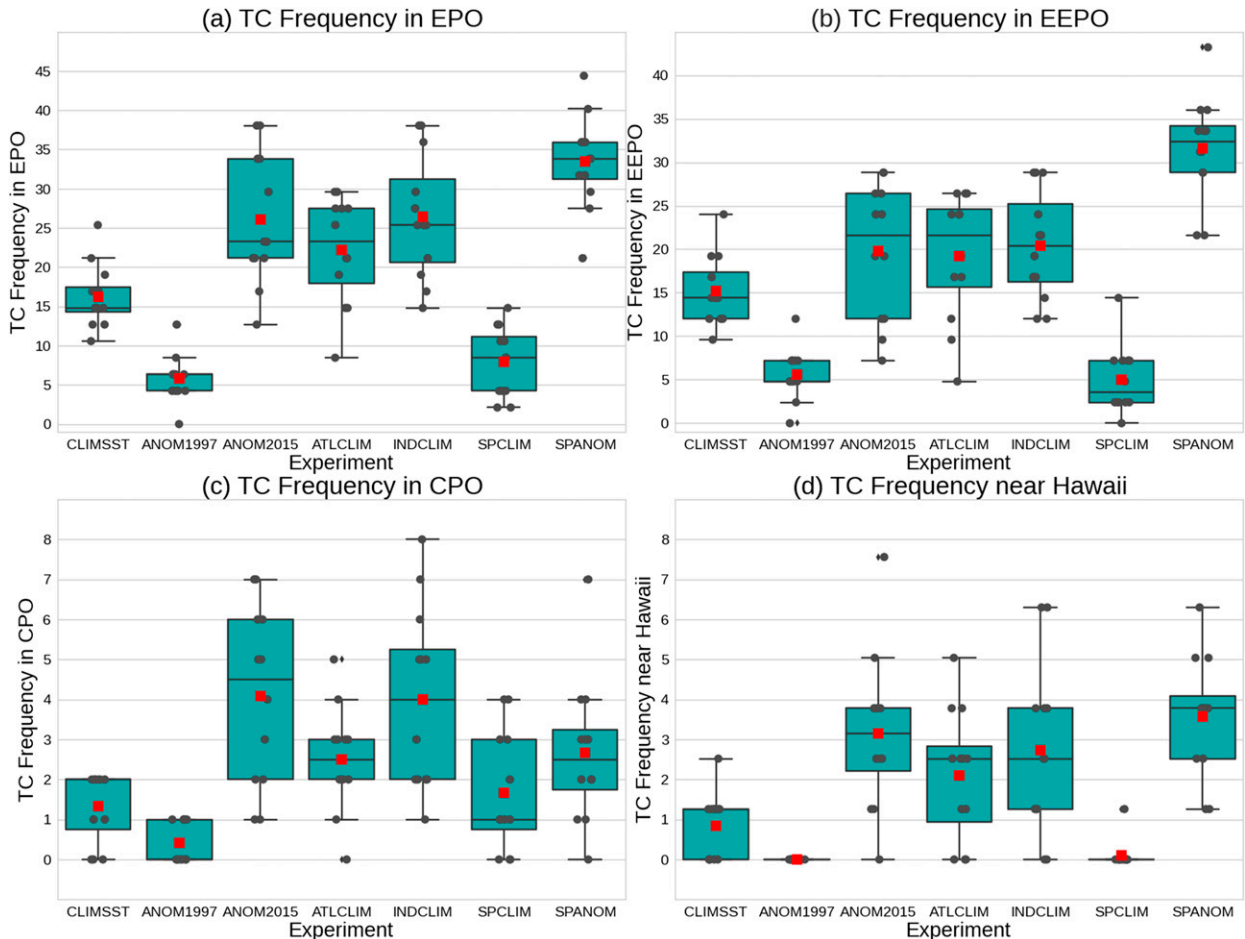


FIG. 10. Box-and-whisker plots for predicted 2015 TC frequency, produced by the atmospheric component of FLOR (AM2.5) with various prescribed SSTA patterns (see text for details) for (a) EPO, (b) EEPO, (c) CPO, and (d) Hawaiian TCs. The red-filled square shows the ensemble mean, whereas the black dots show each ensemble member. The boxes represent the lower and upper quartiles, the horizontal lines in the middle show the median value, and the horizontal end lines show the lowest (highest) datum still within the 1.5 interquartile range (IQR) of the lower (upper) quartile.

shows slight decreases in TC frequency from the ANOM2015 for all of the domains but especially in the CPO, indicating that the cooler Atlantic Ocean influenced the TC activity in the domains through the teleconnection as reported by Kucharski et al. (2011) and Wang and Lee (2009). The SPCLIM experiment is the same as the ANOM2015, except that SSTAs are set to zero north of  $15^{\circ}\text{N}$  in the EPO (Fig. 3c). Conversely, in the SPANOM experiment the SSTA is set to zero everywhere except north of  $10^{\circ}\text{N}$  in the EPO, where the 2015 SSTA is prescribed (Fig. 3d). These idealized experiments show increased TC frequency in response to positive SSTAs over the subtropical EPO.

Note that even though the tropical warm SSTA associated with El Niño is removed in SPANOM, this experiment shows the highest number of storms among the idealized experiments except for the CPO. This suggests

that the 2015 active TC season is more likely attributable to the warm conditions in the subtropical EPO, than those in the tropical EPO. That SPCLIM has even fewer storms than CLIMSST does except for the CPO further suggests that, taken in isolation, the tropical component of the El Niño SSTAs actually suppress TC activity in most of the subdomains. It is possible that some of the SPANOM SSTAs were themselves related to El Niño; indeed they were also evident, to lesser extent, in 1997 (Fig. 3b).

### c. Influence of anthropogenic forcing on occurrence of active TC year like 2015

The previous section highlighted that the subtropical surface warming is a key for the extreme TC year in 2015. On the other hand, a number of state-of-the-art climate models consistently project more warming in the subtropical Pacific relative to the other open oceans

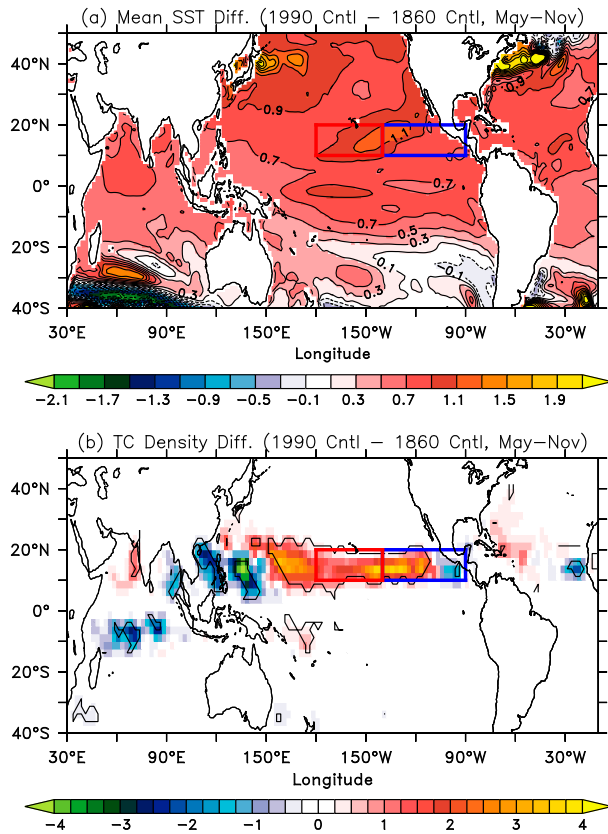


FIG. 11. (a) Projected mean SST difference (K) between 1990-control (500 yr) and 1860-control (3500 yr) experiments during May–November. (b) As in (a), but for projected TC genesis density difference (No. of TCs  $\times 10^{-1}$  for each  $2.5^\circ \times 2.5^\circ$  grid box). Contour line in (b) indicates that the change is statistically significant at the 99% confidence level or above (bootstrap method). The blue and red rectangle domains are defined as the MDRs for TC genesis for the EEPO and CPO, respectively.

(e.g., Xie et al. 2010; Murakami et al. 2013). Therefore, it is possible that anthropogenic forcing might have partially contributed to the extremely warm subsurface ocean in the subtropical Pacific, and that in turn leads to the extreme TC year in 2015. To elucidate the influence of anthropogenic forcing on the probability of occurrence of an extreme TC year such as 2015, we analyzed results from long control runs with forcing fixed at either 1860 conditions (3500-yr simulation) or 1990 conditions (500-yr simulation).

The mean SST difference between these two control experiments is shown in Fig. 11a, revealing relatively higher SST for 1990 conditions in the subtropical EPO; this enhanced subtropical Pacific warming consistently emerges in studies of the response of SSTs to increasing greenhouse gases (Xie et al. 2010; Murakami et al. 2013). Figure 11b shows projected changes in TC genesis density. TC genesis positions are counted for each  $2.5^\circ \times 2.5^\circ$  grid

TABLE 1. Simulated mean TC frequency during May–November for each basin of the EPO, EEPO, CPO, and the Hawaiian region through the control experiments. Statistically significant change at 99% significance level is indicated with an asterisk. A bootstrap method is applied for the test.

Domain	1860-control	1990-control	Diff (1990 – 1860)
EPO	12.0	15.7	+3.7*
EEPO	13.3	15.4	+2.0*
CPO	0.7	1.7	+1.0*
Hawaii	0.2	0.7	+0.5*

box within the global domain. The total count for each grid box is defined as the TC genesis density. It is noted that TC genesis shifts toward the center of the Pacific, which is consistent with the previous studies (Li et al. 2010; Murakami et al. 2013). Over the MDRs in the EPO (blue) and CPO (red), TC genesis is more frequent in the 1990 control experiments than in the 1860 experiment. Table 1 shows mean difference in TC frequency between the 1990- and 1860-control experiments for each domain in the EPO. It shows statistically significant increases in the mean TC frequency for all of the domains.

Projected increase in frequency of occurrence of extremely active TC year is also expected from the projected increase in TC genesis frequency. Following Murakami et al. (2015a), we will examine the empirical probability of exceedance for the frequency of TCs as a function of TC number [i.e.,  $P(x)$ ; see section 2c] in response to anthropogenic radiative forcing changes. Figure 12 shows that the probability of occurrence for an extreme event in the 1990-control than in the 1860-control experiment. Here, extreme range of  $x$  is taken from the value of  $+1\sigma$  for the anomaly of TC frequency based on the 1966–2015 observations (i.e., EPO = 21, EEPO = 19, CPO = 3, and Hawaii = 1). Overall, the probability increases significantly from the 1860-control to the 1990-control for all the domains. The fraction of attributable risk (FAR; Jaeger et al. 2008) is computed for the estimation of the impact of anthropogenic forcing. FAR is defined as follows:

$$\text{FAR}(x) = \frac{P(x|E_1) - P(x|E_0)}{P(x|E_1)}, \quad (3)$$

where  $E_1$  is anthropogenic warming condition, and  $E_0$  is natural forcing alone. FAR ranges from  $-\infty$  (not attributable) to 100% (attributable). In the control experiments, FAR has a range of 60%–80% for the EPO, 40%–60% for the EEPO, 70%–100% for the CPO, and 70%–100% for the Hawaiian domain (green dots in Fig. 12), suggesting that anthropogenic forcing

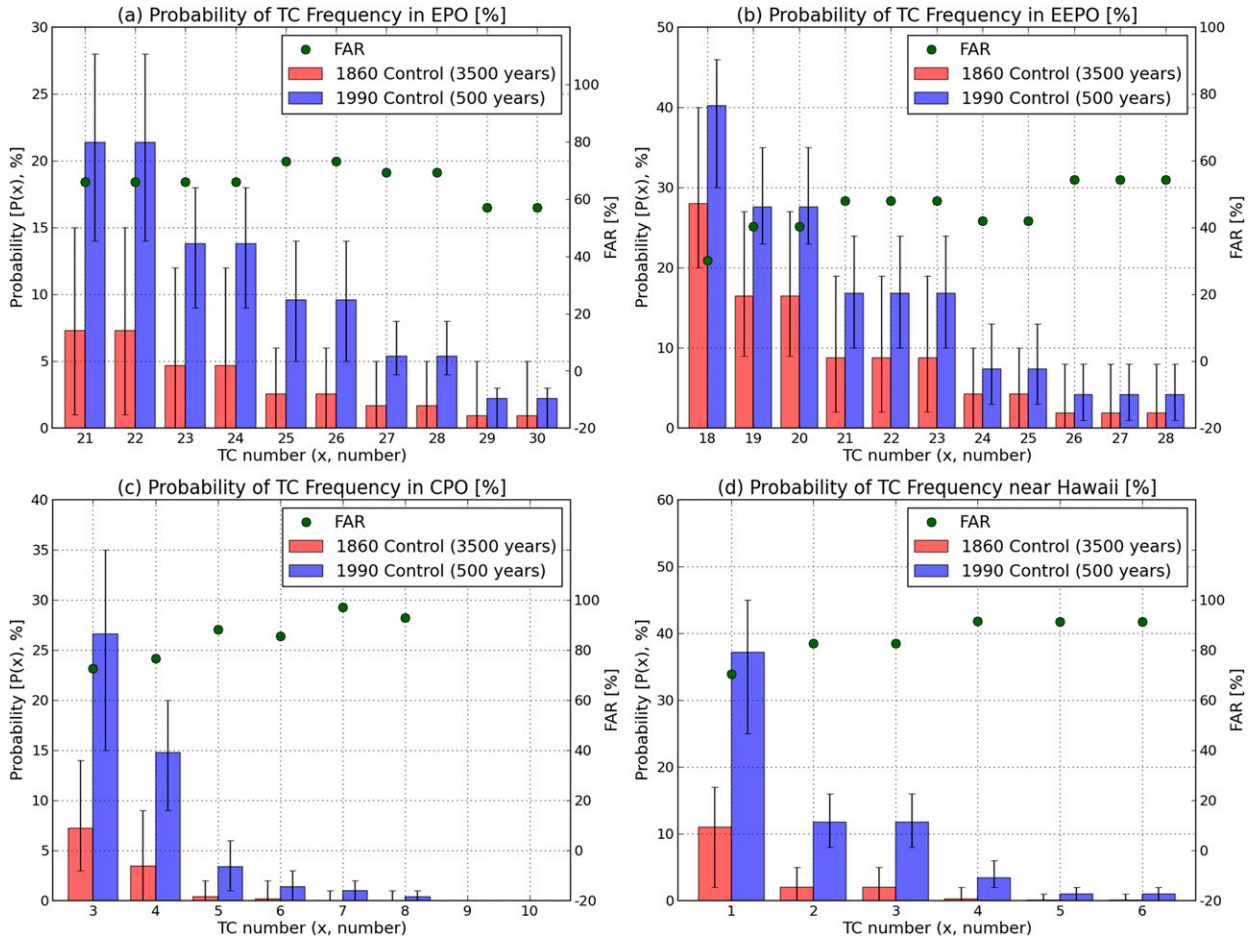


FIG. 12. Results of  $P(x)$  from the control simulations for the (a) EPO, (b) EEPO, (c) CPO, and (d) the Hawaiian domain. The probability of occurrence represented by  $P(x)$  of a year with TC number greater than or equal to  $x$ . Red bars are probability obtained from 1860-control simulation (3500 yr), whereas blue bars are the results from 1990-control simulation (500 yr). Green dots represents FAR computed from Eq. (3).

substantially changes the odds of extreme TC seasons like 2015 relative to natural variability alone.

*d. Influence of internal variability and anthropogenic forcing on occurrence of extreme TC year like 2015*

Generally, more TCs are observed during the positive phase of ENSO (blue), PMM (red), IPO (purple), and PDO (green), and negative phase of AMO (yellow) in the EPO (Fig. 2a). To discriminate the potential influence of natural variability versus anthropogenic forcing on extreme event of TC activity, we analyzed the two 35-member ensembles of simulations, run from 1941 to 2040. In the first ensemble, called AllForc, the simulations were driven by estimates of observed changes in anthropogenic radiative forcing from greenhouse gases and aerosols, as well as projections of future changes based on the RCP4.5 scenario. In the second ensemble, called 1941Forc, the simulations used constant greenhouse gas

and aerosol forcing representative of 1941 conditions. The difference in the mean of the ensembles between the AllForc and 1941Forc is mainly due to the effect of anthropogenic forcing. In addition, responses of the anthropogenic forcing can be estimated by taking mean of the 35 members for the AllForc experiment because the model generated internal variability within each ensemble member is canceled out by the mean operation.

Figure 13 shows the difference in projected mean SST and TC genesis density between the AllForc and 1941Forc experiments for each 20-yr period from 1941. The simulated difference in SST between the AllForc and 1941Forc experiments gradually becomes larger as time proceeds with more warming in the subtropical central Pacific (Figs. 13a–e), which is consistent with the control experiments (Fig. 11a). Impacts of warming on TC genesis density and basin-total TC genesis frequency are generally consistent with those in the control experiments

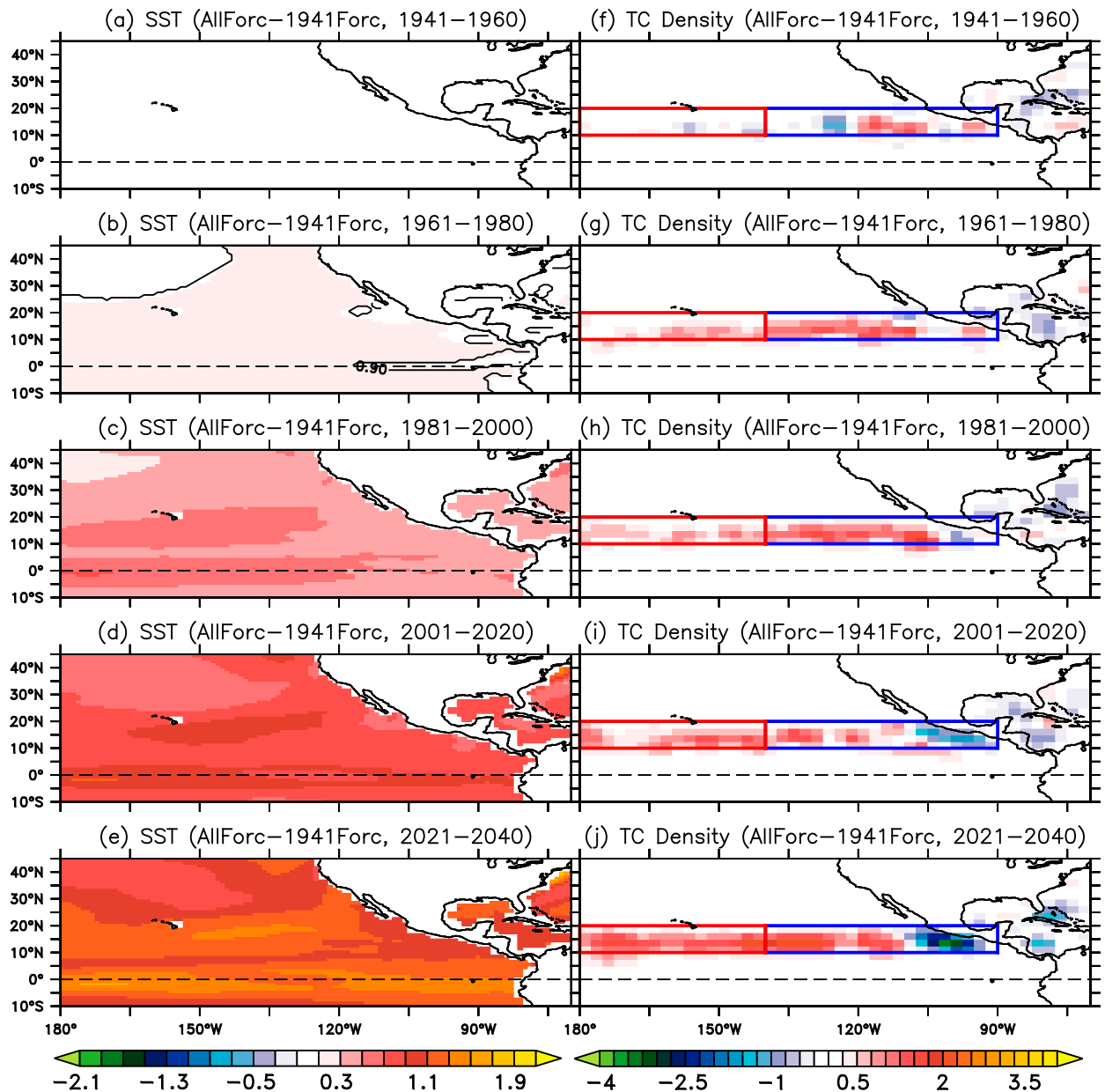


FIG. 13. Difference in (left) simulated mean SST (K) and (right) TC genesis density (No. of TCs  $\times 10^{-1}$  for each  $2.5^{\circ} \times 2.5^{\circ}$  grid box) between the AllForc and 1941Forc experiments for each 20-yr period, for (a),(f) 1941–60, (b),(g) 1961–80, (c),(h) 1981–2000, (d),(i) 2001–20, and (e),(j) 2021–40. The blue and red rectangle domains are defined as the MDRs for TC genesis for the EEPO and CPO, respectively.

(Figs. 13f–j and Table 2): increases of TC genesis frequency in the both EEPO and CPO. A detailed difference from the control experiments is the larger tropical SST anomaly ( $10^{\circ}\text{S}$ – $10^{\circ}\text{N}$ ) during the period 2021–41 that is equivalent to the warming in the subtropical Pacific (Fig. 13e). Another difference is that the decrease in TC genesis density along the coastline of Mexico is larger than that in the control experiments (Figs. 11b, 13j). Consequently, projected changes in basin-total TC genesis frequency in the EEPO for 2001–20 and 2021–41 are

smaller than that in the control experiments, although they are still positive change (Table 2).

Figure 14 summarizes the role of radiative forcing and natural large-scale ocean patterns in altering the probability of occurrence of a hyperactive TC season like that of 2015. Note that because the control experiments did not record nine TCs in the CPO (Fig. 12c), the probability of the occurrence of a year with eight or more TCs is evaluated for the CPO instead. Orange marks in Fig. 14 reveal  $P(x)$  for the fixed forcing control simulations (see

TABLE 2. Simulated mean TC frequency by AllForc experiment during May–November for each 20-yr period for each basin of the EPO, EEPO, CPO, and the Hawaiian region. Numbers in parentheses indicate changes from the value by the 1941Forc experiment. Statistically significant change at 99% significance level is indicated with an asterisk. A bootstrap method is applied for the test.

Domain	1941–60	1961–80	1981–2000	2001–20	2021–40
EPO	15.8 (+0.2)	16.7 (+1.6*)	16.7 (+1.9*)	16.9 (+1.3*)	17.1 (+1.4*)
EEPO	15.1 (+0.3)	15.6 (+1.3*)	15.6 (+1.4*)	15.2 (+0.4)	15.2 (+0.4)
CPO	1.4 (−0.1)	1.7 (+0.4*)	1.7 (+0.4*)	2.0 (+0.5*)	2.3 (+0.8*)
Hawaii	0.5 (−0.1)	0.7 (+0.3*)	0.7 (+0.3*)	1.0 (+0.5*)	1.1 (+0.6*)

section 3c), showing again that the probability of occurrence for an extreme event like that predicted for 2015 is higher in the 1990-control than in the 1860-control experiment. This increased TC incidence is also consistent with the multidecadal simulations, as can be seen by comparing AllForc (black lines) to 1941Forc (gray lines)

in Fig. 14, although the difference in  $P(19)$  for the EEPO is not much clearer between AllForc and 1941Forc, especially after 2000 (Fig. 14b). Therefore, the influence of anthropogenic forcing on the increase in  $P(x)$  is larger in the CPO than in the EEPO. It is interesting that these results are consistent with the 2015 TC season: extreme

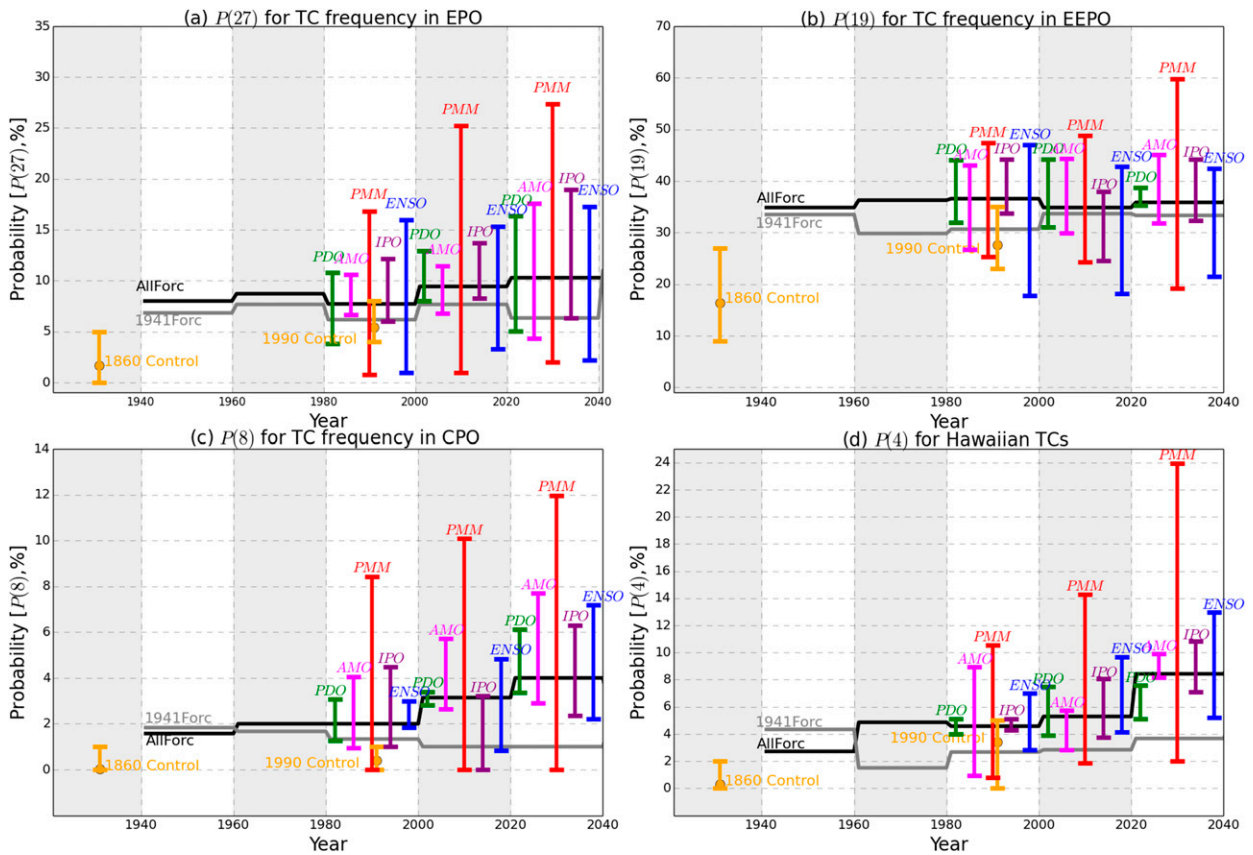


FIG. 14. Probability of equaling or exceeding  $x$  TC occurrences [ $P(x)$ ] between May and November, from a suite of FLOR simulations. Results of (a)  $P(27)$  for TC frequency in the EPO, (b)  $P(19)$  for TC frequency in the EEPO, (c)  $P(8)$  for TC frequency in the CPO, and (d)  $P(4)$  for TC frequency near Hawaii, where exceedance thresholds are determined by the extreme 2015 summer season. For each 20-yr period,  $P(x)$  was calculated from 700 samples based on the time-varying all forcing (AllForc) experiment (black line) and the fixed anthropogenic forcing at 1941 levels (1941Forc) experiment (gray line). Colored bars show the range of conditional  $P(x)$  induced by natural variability computed by the AllForc experiment for each 20-yr period. For example, red bars cover the range of  $P(x | PMM+)$  and  $P(x | PMM-)$ , namely, the range of  $P(x)$  under the conditions between positive and negative PMM phases. Likewise,  $P(x)$  under the condition of positive and negative phases of PDO (green), ENSO (blue), IPO (purple), and AMO (pink) are shown. Orange circles denote results of  $P(x)$  from the control simulations. The orange bars show the range of minimum and maximum when  $P(x)$  is computed for each 100-yr period.

TC frequency in the CPO and moderately active TC season in the EEPO. Overall, the simulations suggest that even subject to a rare confluence of forcings from several natural climate modes, anthropogenic climate change would still have boosted the odds of an extremely active 2015 TC season in the EPO.

The color bars in Fig. 14 reveal the effect of natural variability on the probability of occurrence in the AllForc ensemble members. The relatively wide bars in Fig. 14 highlight the marked influence of natural variability on the probability. In general, for TC incidence in each region, the influences of the PDO and IPO are smaller than those of the PMM and ENSO. On the other hand, the AMO excites larger variability of  $P(x)$  than the PDO and IPO do. It appears that the PMM has the largest influence on the variability of  $P(x)$  in the model experiments. The extremely large number of TCs during the 2015 hurricane season occurred under favorable PMM (+0.9), El Niño (+2.3), and AMO (−1.7). Moreover, defining  $E$  as the event in which the PMM and ENSO indices are all positive and AMO index is negative, as in 2015 (Figs. 2a), we find from the 1990-control that  $P(x|E)$  is about 2.6 (FAR = 61%), 1.3 (FAR = 22%), 6.0 (FAR = 83%), and 7.0 (FAR = 86%) times higher than those from the 1860-control experiment for  $P(27)$  of the EPO TCs,  $P(19)$  of the EEPO TCs,  $P(8)$  of the CPO TCs, and  $P(4)$  of the Hawaiian TCs, respectively. Therefore, it is possible that global warming increased the odds of the extremely large number of the EPO and CPO TCs in 2015 even during the similar conditions of natural variability.

The above discussion does not give any answers as to which of positive PMM and El Niño strictly played the more important role for triggering the extremely active TC year of 2015, because positive PMM sometimes coincides with El Niño. Moreover, Fig. 14 shows that a negative AMO phase provides considerable impact on the variation of  $P(x)$ , especially for the CPO. However, again, some of the negative AMO years coincide with positive PMM and ENSO years. Therefore, we further computed conditional  $P(x)$ , namely,  $P(x|E)$  under the five conditions of E1–E5 in order to strictly separate the effect of the single natural variability from others. The condition E1 is the combined condition when  $\text{PMM} \geq +1\sigma$ ,  $\text{Niño-3.4} \geq +1\sigma$ , and  $\text{AMO} \leq -1\sigma$ , implying similar condition to the 2015 summer season. E2 is for the years with  $\text{PMM} \geq +1\sigma$ , but  $\text{Niño-3.4} < +1\sigma$  and  $\text{AMO} > -1\sigma$ , as an indication of PMM-only effect by excluding the El Niño and negative AMO. E3 is for the years when  $\text{Niño-3.4} \geq +1\sigma$ , but  $\text{PMM} < +1\sigma$  and  $\text{AMO} > -1\sigma$ , namely, an El Niño-only effect. E4 is for the years when  $\text{AMO} \leq -1\sigma$ , but  $\text{PMM} < +1\sigma$  and  $\text{Niño-3.4} < +1\sigma$ , as an indication of

an AMO-only effect. E5 is for the years with  $\text{PMM} < +1\sigma$ ,  $\text{Niño-3.4} < +1\sigma$ , and  $\text{AMO} > -1\sigma$ , representing no effect. Figure 15 shows the conditional probability of exceedance using the AllForc experiment for the 2001–20 period in which 2015 is included. Figure 15 highlights that the  $P(x|E1)$  is the highest for most of the basins and most of the TC numbers, as expected. Moreover,  $P(x|E2)$  is much larger than  $P(x|E3)$  and  $P(x|E4)$ , in addition to that  $P(x|E2)$  is closer to  $P(x|E1)$ . This indicates that the odds of occurrence of the extreme TC event in the EPO, EEPO, CPO, and the Hawaiian domain increase a lot by the positive PMM only. FAR is computed from the basis of E5 [i.e.,  $E_0 = E5$  in Eq. (3)] in Fig. 15. FAR is about 60%–80% for E2 in the EPO (blue circles), whereas that is about 20%–40% for E3 (green circles) and 0% or negative for E4 (pink circles) in the EPO. And above results are generally and qualitatively consistent for the EEPO (Fig. 15b), CPO (Fig. 15c), and the Hawaiian domain (Fig. 15d). Therefore, the 2015 extreme TC events may be due mostly to the positive PMM (namely, the subtropical Pacific warming) rather than the tropical Pacific warming by the strong El Niño and the tropical Atlantic cooling by the negative AMO phase. Because FAR is still about 20%–40% for E3 for the EPO (Fig. 15a), we cannot completely rule out the effect of the strong El Niño on the emergence of the extremely active TC season in 2015. However, from the above discussions, it is likely that the positive PMM gave a larger impact on the active TC season in the EPO than the strong El Niño did.

#### 4. Conclusions and discussion

The 2015 hurricane season in the EPO and CPO, particularly around Hawaii, was extremely active. There was a historical record of 27 (9) TCs observed in the EPO (CPO). In addition, three hurricanes approached Hawaiian Islands in that year. The Niño-3.4 index was also high in the 2015 summer season. The observed co-occurrence of an active TC season and the strong El Niño in the EPO brought scientific arguments whether the active 2015 TC year arose by the strong El Niño development.

However, the observed record since 1966 shows that the extremely active TC years in the EPO do not always arise during the tropical Pacific warming years (i.e., El Niño years). Meanwhile, they arise more frequently during the subtropical Pacific warming years than the tropical Pacific warming years. Moreover, reanalysis data show that the large-scale conditions are more favorable for TC genesis over the MDRs for the EEPO and CPO during the subtropical Pacific warming years than the tropical Pacific warming years. The positive

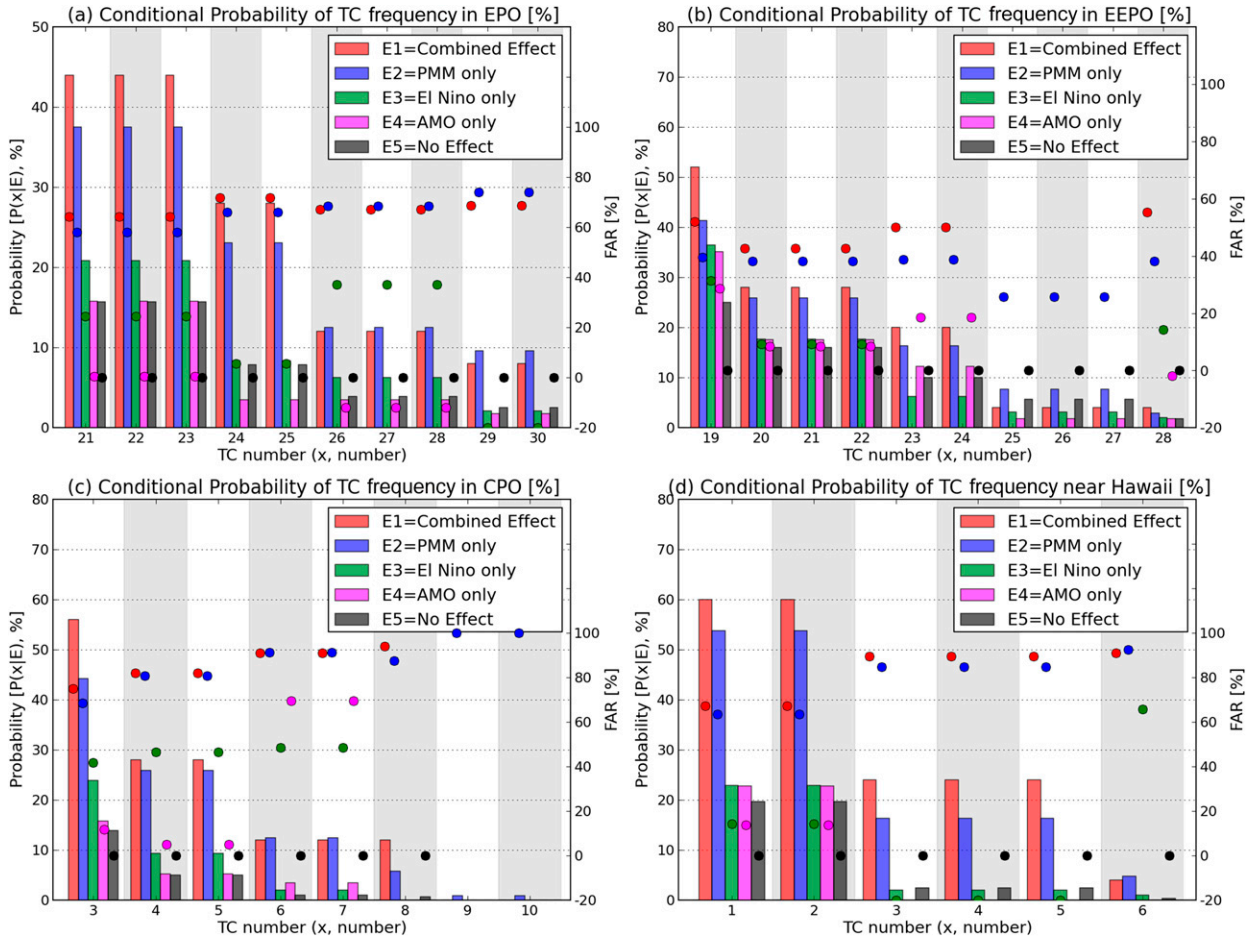


FIG. 15. As in Fig. 12, but for the results of the conditional probability of exceedance  $P(x | E)$  for the period of 2001–20 from the AllForc multidecadal simulation. See text for the definitions of conditions E1–E5. FAR (dots) is computed from the basis of E5 [i.e.,  $E_0 = E_5$  in Eq. (3)], indicating the impact of the single natural variability on the variation of probability of exceedance relative to that without PMM, El Niño, and AMO. Sample size for each condition is 25, 104, 96, 57, and 280 for E1, E2, E3, E4, and E5, respectively, from the total sample of 700 (during the 20 yr with the 35 ensemble members).

SSTA over the subtropical EPO in 2015 is mainly associated with the positive phase of PMM, with some possible contributions from the decadal variation of PDO, IPO, and AMO. Moreover, the state-of-the-art climate models commonly project substantial subtropical Pacific warming in the future by anthropogenic forcing. Therefore, we hypothesize that the active 2015 TC season in the EPO was mostly caused by the subtropical Pacific warming mostly associated with the internal variability of positive PMM phase, superimposed on the anthropogenic global warming effect, rather than the tropical Pacific warming associated with El Niño development.

To support the hypothesis, the suite of fixed forcing control simulations, seasonal predictions, and multidecadal simulations were conducted using FLOR and AM2.5. These results suggest that the extreme TC frequency in 2015 was mainly linked to a positive PMM,

with a weaker link to El Niño. Furthermore, the model experiments indicate that the impact of the PMM on the EPO, EEPO, CPO, and the Hawaiian TCs in 2015 occurred in the context of an underlying increase in the probability of years with extreme TC activity due to anthropogenic forcing. The projected probability of exceedance continues to increase through 2020–40 in the EPO due to anthropogenic forcing, especially for the CPO and the Hawaiian domain—arising in large part due to projections for an enhanced surface warming in the subtropical Pacific in response to increasing greenhouse gases (Vecchi and Soden 2007; Xie et al. 2010; Li et al. 2010; Murakami et al. 2013). Moreover, the natural decadal variability of the IPO and PDO might have also changed sign recently (Fig. 2), leading to more favorable conditions for the occurrence of an extremely active TC year in the EPO. Klotzbach et al. (2015) also reported that the AMO

might have switched phase to negative in 2014 or 2015 (Fig. S5 in the supplemental material). Therefore, it is possible that the change in AMO phase might have caused the active 2015 TC year. However, further analysis for the multidecadal simulations showed that the negative AMO alone did not influence the increase of probability of occurrence of the active TC season like 2015 for all of the ocean basins. It is positive PMM alone that caused the increase of the probability of extreme TC season rather than El Niño and negative AMO. These results indicate that extreme years, like 2015, are likely to become more common in the near future, although subject to strong intrinsic modulation arising mainly from the PMM.

We stress that our finding is a model-based attribution and does not constitute a detectable anthropogenic influence at this stage. In particular, the relatively short (~50 yr) time series of the observed TC frequency in the EPO, EEPO, CPO, and the area near Hawaii do not show a rising trend over time (Fig. 2). This lack of detection may be due to the pronounced internal climate variability of TC occurrence in these regions, or it could indicate a deficiency in the modeled sensitivity of TCs in the EPO, EEPO, CPO, and Hawaii. Assessment of model-based attribution, and related projection, would benefit immensely from a longer relatively homogeneous record of the EPO, EEPO, CPO, and Hawaiian TCs, as presently exists for the Atlantic (Landsea et al. 2004, 2010).

**Acknowledgments.** The authors thank Dr. Shukuro Manabe, Dr. Thomas R. Knutson, and Dr. Nathaniel Johnson for their suggestions and comments. This report was prepared by HM under Award NA14OAR4830101 from the National Oceanic and Atmospheric Administration, U.S. Department of Commerce. The statements, findings, conclusions, and recommendations are those of the authors and do not necessarily reflect the views of the National Oceanic and Atmospheric Administration, or the U.S. Department of Commerce.

#### REFERENCES

- Chang, P., L. Zhang, R. Saravanan, D. J. Vimont, J. C. H. Chiang, L. Ji, H. Seidel, and M. K. Tippet, 2007: Pacific meridional mode and El Niño–Southern Oscillation. *Geophys. Res. Lett.*, **34**, L16608, doi:10.1029/2007GL030302.
- Chang, Y.-S., S. Zhang, A. Rosati, T. L. Delworth, and W. F. Stern, 2013: An assessment of oceanic variability for 1960–2010 from the GFDL ensemble coupled data assimilation. *Climate Dyn.*, **40**, 775–803, doi:10.1007/s00382-012-1412-2.
- Chiang, J. C. H., and D. J. Vimont, 2004: Analogous Pacific and Atlantic meridional modes of tropical atmosphere–ocean variability. *J. Climate*, **17**, 4143–4158, doi:10.1175/JCLI4953.1.
- Chu, P.-S., 2004: ENSO and tropical cyclone activity. *Hurricanes and Typhoons: Past, Present, and Potential*, R. J. Murnane and K.-B. Liu, Eds., Columbia University Press, 297–332.
- , and J. Wang, 1997: Tropical cyclone occurrences in the vicinity of Hawaii: Are the differences between El Niño and non-El Niño years significant? *J. Climate*, **10**, 2683–2689, doi:10.1175/1520-0442(1997)010<2683:TCOITV>2.0.CO;2.
- , and J. D. Clark, 1999: Decadal variations of tropical cyclone activity over the central North Pacific. *Bull. Amer. Meteor. Soc.*, **80**, 1875–1881, doi:10.1175/1520-0477(1999)080<1875:DVOTCA>2.0.CO;2.
- Collins, J. M., and D. R. Roache, 2011: The 2009 hurricane season in the eastern North Pacific basin: An analysis of environmental conditions. *Mon. Wea. Rev.*, **139**, 1673–1682, doi:10.1175/2010MWR3538.1.
- Delworth, T. L., and M. E. Mann, 2000: Observed and simulated multidecadal variability in the Northern Hemisphere. *Climate Dyn.*, **16**, 661–676, doi:10.1007/s003820000075.
- , and Coauthors, 2006: GFDL's CM2 global coupled climate models. Part I: Formulation and simulation characteristics. *J. Climate*, **19**, 643–674, doi:10.1175/JCLI3629.1.
- , F. Zeng, A. Rosati, G. A. Vecchi, and A. T. Wittenberg, 2015: A link between the hiatus in global warming and North American drought. *J. Climate*, **28**, 3834–3845, doi:10.1175/JCLI-D-14-00616.1.
- Deser, C., and M. L. Blackmon, 1995: On the relationship between tropical and North Pacific sea surface temperature variations. *J. Climate*, **8**, 1677–1680, doi:10.1175/1520-0442(1995)008<1677:OTRBT>2.0.CO;2.
- Di Liberto, T., 2015: Central Pacific hurricane party: Three's company. *ClimateWatch*, posted 3 September 2015. [Available online at <https://www.climate.gov/news-features/event-tracker/central-pacific-hurricane-party-three-s-company>.]
- England, M. H., and Coauthors, 2014: Recent intensification of wind-driven circulation in the Pacific and the ongoing warming hiatus. *Nat. Climate Change*, **4**, 222–227, doi:10.1038/nclimate2106.
- Folland, C. K., J. A. Renwick, M. J. Salinger, and A. B. Mullan, 2002: Relative influences of the interdecadal Pacific oscillation and ENSO on the South Pacific convergence zone. *Geophys. Res. Lett.*, **29**, 211–214, doi:10.1029/2001GL014201.
- Frank, W. M., 1987: Tropical cyclone formation. *A Global View of Tropical Cyclones*, R. L. Elsberry et al., Eds., Naval Postgraduate School, 53–90.
- Gnanadesikan, A., and Coauthors, 2006: GFDL's CM2 global coupled climate models. Part II: The baseline ocean simulation. *J. Climate*, **19**, 675–697, doi:10.1175/JCLI3630.1.
- Gray, W. M., 1975: Tropical cyclone genesis. Colorado State University Dept. of Atmospheric Science Paper 234, 121 pp.
- Harris, L. M., S.-J. Lin, and C. Y. Tu, 2016: High-resolution climate simulations using GFDL HiRAM with a stretched global grid. *J. Climate*, **29**, 4293–4314, doi:10.1175/JCLI-D-15-0389.1.
- Hartmann, D. L., 2015: Pacific sea surface temperature and the winter of 2014. *Geophys. Res. Lett.*, **42**, 1894–1902, doi:10.1002/2015GL063083.
- Jaeger, C. C., J. Krause, A. Haas, R. Klein, and K. Hasselmann, 2008: A method for computing the fraction of attributable risk related to climate damages. *Risk Anal.*, **28**, 815–823, doi:10.1111/j.1539-6924.2008.01070.x.
- Jia, L., and Coauthors, 2015: Improved seasonal prediction of temperature and precipitation over land in a high-resolution GFDL climate model. *J. Climate*, **28**, 2044–2062, doi:10.1175/JCLI-D-14-00112.1.
- , and Coauthors, 2016: The roles of radiative forcing, sea surface temperatures, and atmospheric and land initial conditions in U.S. summer warming episodes. *J. Climate*, **29**, 4121–4135, doi:10.1175/JCLI-D-15-0471.1.

- Jin, F.-F., J. Boucharel, and I.-I. Lin, 2014: Eastern Pacific tropical cyclone intensified by El Niño delivery of subsurface ocean heat. *Nature*, **516**, 82–85, doi:10.1038/nature13958.
- Kim, H.-S., G. A. Vecchi, T. R. Knutson, W. G. Anderson, T. L. Delworth, A. Rosati, F. Zeng, and M. Zhao, 2014: Tropical cyclone simulation and response to CO<sub>2</sub> doubling in the GFDL CM2.5 high-resolution coupled climate model. *J. Climate*, **27**, 8034–8054, doi:10.1175/JCLI-D-13-00475.1.
- Klotzbach, P., W. Gray, and C. Fogarty, 2015: Active Atlantic hurricane era at its end? *Nat. Geosci.*, **8**, 737–738, doi:10.1038/ngeo2529.
- Knapp, K. R., M. C. Kruk, D. H. Levinson, H. J. Diamond, and C. J. Neuman, 2010: The International Best Track Archive for Climate Stewardship (IBTrACS): Unifying tropical cyclone data. *Bull. Amer. Meteor. Soc.*, **91**, 363–376, doi:10.1175/2009BAMS2755.1.
- Knutson, T. R., J. J. Sirutis, M. Zhao, R. E. Tuleya, M. Bender, G. A. Vecchi, G. Villarini, and D. Chavas, 2015: Global projections of intense tropical cyclone activity for the late twenty-first century from dynamical downscaling of CMIP5/RCP4.5 scenarios. *J. Climate*, **28**, 7203–7224, doi:10.1175/JCLI-D-15-0129.1.
- Kobayashi, S., and Coauthors, 2015: The JRA-55 reanalysis: General specifications and basic characteristics. *J. Meteor. Soc. Japan*, **93**, 5–48, doi:10.2151/jmsj.2015-001.
- Krishnamurthy, L., G. A. Vecchi, R. Msadek, A. Wittenberg, T. Delworth, and F. Zeng, 2015: The seasonality of the Great Plains low-level jet and ENSO relationship. *J. Climate*, **28**, 4525–4544, doi:10.1175/JCLI-D-14-00590.1.
- , —, —, H. Murakami, A. Wittenberg, and F. Zeng, 2016: Impact of strong ENSO on regional tropical cyclone activity in a high-resolution climate model in the North Pacific and North Atlantic Oceans. *J. Climate*, **29**, 2375–2394, doi:10.1175/JCLI-D-15-0468.1.
- Kucharski, K., I.-S. Kang, R. Farneti, and L. Feudale, 2011: Tropical Pacific response to 20th century Atlantic warming. *Geophys. Res. Lett.*, **38**, L03702, doi:10.1029/2010GL046248.
- Landsea, C. W., and J. L. Franklin, 2013: Atlantic hurricane database uncertainty and presentation of a new database format. *Mon. Wea. Rev.*, **141**, 3576–3592, doi:10.1175/MWR-D-12-00254.1.
- , and Coauthors, 2004: The Atlantic hurricane database reanalysis project: Documentation for the 1851–1910 alterations and additions to the HURDAT database. *Hurricanes and Typhoons: Past, Present and Future*, R. J. Murname and K.-B. Liu, Eds., Columbia University Press, 177–221.
- , G. A. Vecchi, L. Bengtsson, and T. R. Knutson, 2010: Impact of duration thresholds on Atlantic tropical cyclone counts. *J. Climate*, **23**, 2508–2519, doi:10.1175/2009JCLI3034.1.
- Larson, S. M., S.-K. Lee, C. Wang, E.-S. Chung, and D. Enfield, 2012: Impacts of non-canonical El Niño patterns on Atlantic hurricane activity. *Geophys. Res. Lett.*, **39**, L14706, doi:10.1029/2012GL052595.
- Li, T., M. Kwon, M. Zhao, J.-S. Kug, J.-J. Luo, and W. Yu, 2010: Global warming shifts Pacific tropical cyclone location. *Geophys. Res. Lett.*, **37**, L21804, doi:10.1029/2010GL045124.
- Lupo, A. R., T. K. Latham, T. Magill, J. V. Clark, C. J. Melick, and P. S. Market, 2008: The interannual variability of hurricane activity in the Atlantic and East Pacific regions. *Natl. Wea. Dig.*, **32**, 119–135.
- Mantua, N. J., S. R. Hare, Y. Zhang, J. M. Wallace, and R. C. Francis, 1997: A Pacific interdecadal climate oscillation with impacts on salmon production. *Bull. Amer. Meteor. Soc.*, **78**, 1069–1079, doi:10.1175/1520-0477(1997)078<1069:APICOW>2.0.CO;2.
- Merlis, T. M., M. Zhao, and I. M. Held, 2013: The sensitivity of hurricane frequency to ITCZ changes and radiatively forced warming in aquaplanet simulations. *Geophys. Res. Lett.*, **40**, 4109–4114, doi:10.1002/grl.50680.
- Msadek, R., G. A. Vecchi, M. Winton, and R. G. Gudgel, 2014: Importance of initial conditions in seasonal predictions of Arctic sea ice extent. *Geophys. Res. Lett.*, **41**, 5208–5215, doi:10.1002/2014GL060799.
- Murakami, H., B. Wang, T. Li, and A. Kitoh, 2013: Projected increase in tropical cyclones near Hawaii. *Nat. Climate Change*, **3**, 749–754, doi:10.1038/nclimate1890.
- , G. A. Vecchi, T. L. Delworth, K. Paffendorf, R. Gudgel, L. Jia, and F. Zeng, 2015a: Investigating the influence of anthropogenic forcing and natural variability on the 2014 Hawaiian hurricane season [in “Explaining Extremes of 2014 from a Climate Perspective”]. *Bull. Amer. Meteor. Soc.*, **96**, S115–S119, doi:10.1175/BAMS-D-15-00119.1.
- , and Coauthors, 2015b: Simulation and prediction of category 4 and 5 hurricanes in the high-resolution GFDL HiFLOR coupled climate model. *J. Climate*, **28**, 9058–9079, doi:10.1175/JCLI-D-15-0216.1.
- , G. Villarini, G. A. Vecchi, W. Zhang, and R. Gudgel, 2016a: Statistical–dynamical seasonal forecast of North Atlantic and U.S. landfalling tropical cyclones using the high-resolution GFDL FLOR coupled model. *Mon. Wea. Rev.*, **144**, 2101–2123, doi:10.1175/MWR-D-15-0308.1.
- , and Coauthors, 2016b: Seasonal forecasts of major hurricanes and landfalling tropical cyclones using a high-resolution GFDL coupled climate model. *J. Climate*, **29**, 7977–7989, doi:10.1175/JCLI-D-16-0233.1.
- Power, S., T. Casey, C. Folland, A. Colman, and V. Mehta, 1999: Interdecadal modulation of the impact of ENSO on Australia. *Climate Dyn.*, **15**, 319–324, doi:10.1007/s003820050284.
- Rayner, N. A., D. E. Parker, E. B. Horton, C. K. Folland, L. V. Alexander, and D. P. Rowell, 2003: Global analysis of sea surface temperature, sea ice, and night marine air temperature since the late nineteenth century. *J. Geophys. Res.*, **108**, 4407, doi:10.1029/2002JD002670.
- The Weather Channel, 2015: Three category 4 hurricanes in the Pacific Ocean: How rare is that? The Weather Channel, accessed November 2015. [Available online at <http://www.weather.com/storms/hurricane/news/three-category-4-hurricanes-pacific-kilo-ignacio-jimena>.]
- Thompson, A., 2015: El Niño helps boost Pacific storm season. Accessed November 2015. [Available online at <http://www.climatecentral.org/news/el-nino-boosts-pacific-storms-19210>.]
- Unisys, 2016: Unisys weather hurricane tropical data. Accessed January 2016. [Available online at <http://weather.unisys.com/hurricane/>.]
- Vecchi, G. A., and B. J. Soden, 2007: Effect of remote sea surface temperature change on tropical cyclone potential intensity. *Nature*, **450**, 1066–1070, doi:10.1038/nature06423.
- , and Coauthors, 2014: On the seasonal forecasting of regional tropical cyclone activity. *J. Climate*, **27**, 7994–8016, doi:10.1175/JCLI-D-14-00158.1.
- Wang, B., Y. Yang, Q.-H. Ding, H. Murakami, and F. Huang, 2010: Climate control of the global tropical storm days (1965–2008). *Geophys. Res. Lett.*, **37**, L07704, doi:10.1029/2010GL042487.
- Wang, C., and S.-K. Lee, 2009: Co-variability of tropical cyclones in the North Atlantic and the eastern North Pacific. *Geophys. Res. Lett.*, **36**, L24702, doi:10.1029/2009GL041469.
- Whitney, L. D., and J. Hobgood, 1997: The relationship between sea surface temperatures and maximum intensities of tropical cyclones in the eastern North Pacific Ocean. *J. Climate*, **10**, 2921–2930, doi:10.1175/1520-0442(1997)010<2921:TRBSST>2.0.CO;2.

- Winton, M., W. G. Anderson, T. L. Delworth, S. M. Griffies, W. J. Hurlin, and A. Rosati, 2014: Has coarse ocean resolution biased simulations of transient climate sensitivity? *Geophys. Res. Lett.*, **41**, 8522–8529, doi:[10.1002/2014GL061523](https://doi.org/10.1002/2014GL061523).
- Wittenberg, A. T., A. Rosati, N.-C. Lau, and J. J. Ploshay, 2006: GFDL's CM2 global coupled climate models. Part III: Tropical Pacific climate and ENSO. *J. Climate*, **19**, 698–722, doi:[10.1175/JCLI3631.1](https://doi.org/10.1175/JCLI3631.1).
- Wu, P., and P.-S. Chu, 2007: Characteristics of tropical cyclone activity over the eastern North Pacific: The extremely active 1992 and the inactive 1997. *Tellus*, **59A**, 444–454, doi:[10.1111/j.1600-0870.2007.00248.x](https://doi.org/10.1111/j.1600-0870.2007.00248.x).
- Xie, P., and P. A. Arkin, 1997: Global precipitation: A 17-year monthly analysis based on gauge observations, satellite estimates, and numerical model outputs. *Bull. Amer. Meteor. Soc.*, **78**, 2539–2558, doi:[10.1175/1520-0477\(1997\)078<2539:GPAYMA>2.0.CO;2](https://doi.org/10.1175/1520-0477(1997)078<2539:GPAYMA>2.0.CO;2).
- Xie, S.-P., C. Deser, G. A. Vecchi, J. Ma, H. Teng, and A. T. Wittenberg, 2010: Global warming pattern formation: Sea surface temperature and rainfall. *J. Climate*, **23**, 966–986, doi:[10.1175/2009JCLI3329.1](https://doi.org/10.1175/2009JCLI3329.1).
- Yang, X., and Coauthors, 2015a: Seasonal predictability of extratropical storm tracks in GFDL's high-resolution climate prediction model. *J. Climate*, **28**, 3592–3611, doi:[10.1175/JCLI-D-14-00517.1](https://doi.org/10.1175/JCLI-D-14-00517.1).
- , G. A. Vecchi, T. L. Delworth, K. Paffendorf, L. Jia, R. Gudgel, F. Zeng, and S. D. Underwood, 2015b: Extreme North America winter storm season of 2013/14: Roles of radiative forcing and the global warming hiatus [in “Explaining Extremes of 2014 from a Climate Perspective”]. *Bull. Amer. Meteor. Soc.*, **96**, S25–S28, doi:[10.1175/BAMS-D-15-00133.1](https://doi.org/10.1175/BAMS-D-15-00133.1).
- Zhang, L., P. Chang, and L. Ji, 2009: Linking the Pacific meridional mode to ENSO: Coupled model analysis. *J. Climate*, **22**, 3488–3505, doi:[10.1175/2008JCLI2473.1](https://doi.org/10.1175/2008JCLI2473.1).
- Zhang, L. P., and T. L. Delworth, 2015: Analysis of the characteristics and mechanisms of the Pacific decadal oscillation in a suite of coupled models from the Geophysical Fluid Dynamics Laboratory. *J. Climate*, **28**, 7678–7701, doi:[10.1175/JCLI-D-14-00647.1](https://doi.org/10.1175/JCLI-D-14-00647.1).
- Zhang, S., and A. Rosati, 2010: An inflated ensemble filter for ocean data assimilation with a biased coupled GCM. *Mon. Wea. Rev.*, **138**, 3905–3931, doi:[10.1175/2010MWR3326.1](https://doi.org/10.1175/2010MWR3326.1).
- Zhang, W., and Coauthors, 2016a: Improved simulation of tropical cyclone responses to ENSO in the western North Pacific in the high-resolution GFDL HiFLOR coupled climate model. *J. Climate*, **29**, 1391–1415, doi:[10.1175/JCLI-D-15-0475.1](https://doi.org/10.1175/JCLI-D-15-0475.1).
- , G. Villarini, G. A. Vecchi, H. Murakami, and R. Gudgel, 2016b: Statistical–dynamical seasonal forecast of western North Pacific and East Asia landfalling tropical cyclones using the high-resolution GFDL FLOR coupled model. *J. Adv. Model. Earth Syst.*, **8**, 538–565, doi:[10.1002/2015MS000607](https://doi.org/10.1002/2015MS000607).